

## A geometry projection method for the topology optimization of additively manufactured variable-stiffness composite laminates

Gandhi, Yogesh; Aragón, Alejandro M.; Norato, Julián; Minak, Giangiacomo

**DOI**

[10.1016/j.cma.2024.117663](https://doi.org/10.1016/j.cma.2024.117663)

**Publication date**

2025

**Document Version**

Final published version

**Published in**

Computer Methods in Applied Mechanics and Engineering

**Citation (APA)**

Gandhi, Y., Aragón, A. M., Norato, J., & Minak, G. (2025). A geometry projection method for the topology optimization of additively manufactured variable-stiffness composite laminates. *Computer Methods in Applied Mechanics and Engineering*, 435, Article 117663. <https://doi.org/10.1016/j.cma.2024.117663>

**Important note**

To cite this publication, please use the final published version (if applicable). Please check the document version above.

**Copyright**

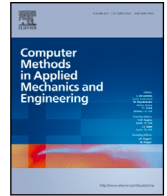
Other than for strictly personal use, it is not permitted to download, forward or distribute the text or part of it, without the consent of the author(s) and/or copyright holder(s), unless the work is under an open content license such as Creative Commons.

**Takedown policy**





Please contact us and provide details if you believe this document breaches copyrights. We will remove access to the work immediately and investigate your claim.

Contents lists available at [ScienceDirect](https://www.sciencedirect.com)

Comput. Methods Appl. Mech. Engrg.

journal homepage: [www.elsevier.com/locate/cma](http://www.elsevier.com/locate/cma)

# A geometry projection method for the topology optimization of additively manufactured variable-stiffness composite laminates

Yogesh Gandhi <sup>a</sup><sup>\*</sup>, Alejandro M. Aragón <sup>b</sup>, Julián Norato <sup>c</sup>,  
Giangiacomo Minak <sup>a</sup>

<sup>a</sup> Department of Industrial Engineering, University of Bologna, Via Fontanelle, 40, Forlì, 47121, Italy

<sup>b</sup> Faculty of Mechanical Engineering, Delft University of Technology, Mekelweg 2, Delft, 2628 CD, The Netherlands

<sup>c</sup> School of Mechanical, Aerospace, and Manufacturing Engineering, University of Connecticut, 191 Auditorium Road, U-3139, Storrs, CT 06269, USA

## ARTICLE INFO

### Keywords:

Topology optimization  
Geometry projection  
Continuous fiber-reinforced polymers  
Variable-stiffness laminates  
Fused filament fabrication

## ABSTRACT

Continuous fiber fused filament fabrication (CF4) is a layer-by-layer additive manufacturing technique that deposits continuous fiber fused filaments (CFFFs) with a significant in-plane variation of the fiber trajectory, thereby offering great flexibility in fabricating variable-stiffness composite laminates (VSCLs). We introduce a topology optimization method for the design of additively manufactured VSCLs made of overlapping, fiber-reinforced bars. The proposed method is based on geometry projection (GP) techniques, whereby the bars are represented by high-level geometric primitives. As in other GP techniques, this high-level parameterization is mapped onto a fixed structured finite element mesh for conducting analysis, as in density-based topology optimization techniques. However, unlike previous GP techniques that have demonstrated their applicability in designing structures as assemblies of individual fiber-reinforced components, this work focuses on the design of composite structures that adhere to CF4 manufacturing processes. Therefore, we first formulate a material interpolation scheme that better captures the stiffness at the composite's joints obtained from bar overlaps as a stack. Second, the proposed material interpolation employs composite laminate theory to capture the in-plane and out-of-plane behavior of the structure. Third, to produce designs that conform to the CF4 process, we also proposed a novel length constraint formulation in the form of penalization on the projection scheme, which ensures a minimum length for all the bars. This minimum length limit does not require adding a constraint to the optimization problem. The efficacy and efficiency of the proposed method are demonstrated by a series of compliance minimization problems with in-plane and/or out-of-plane loading. The methodology is also applied to the design of a displacement inverter compliant mechanism.

## 1. Introduction

Several additive manufacturing methods are being developed to realize the next-generation lightweight composite structures, including variable stiffness composite laminates (VSCLs) made of continuous fiber-reinforced polymers (CFRPs). Some of these methods include continuous fiber-fused filament fabrication (CF4) [1] and automated fiber placement (AFP) [2], which can realize spatially varying material fractions and orientations that can further tailor the VSCLs' mechanical behavior. However, manufacturing

\* Corresponding author.

E-mail address: [yogesh.gandhi@unibo.it](mailto:yogesh.gandhi@unibo.it) (Y. Gandhi).

<https://doi.org/10.1016/j.cma.2024.117663>

Received 9 August 2024; Received in revised form 13 November 2024; Accepted 7 December 2024

Available online 24 December 2024

0045-7825/© 2024 The Authors. Published by Elsevier B.V. This is an open access article under the CC BY-NC-ND license (<http://creativecommons.org/licenses/by-nc-nd/4.0/>).

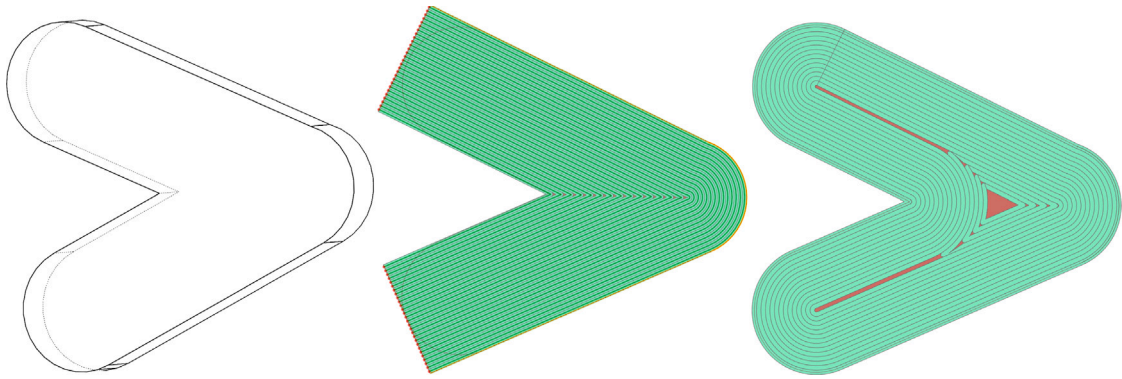


**Fig. 1.** Simple part modeled (on the left) to illustrate the CFFF trajectories that can be deposited in a layer using the CF4 3D-printer from 9tllabs. The CFFF trajectories (obtained using 9tllabs's slicing software Fibrify<sup>®</sup>) can be laid horizontally and continuously in a layer, in an “line follower” (middle) or “face follower” (right) pattern. The line follower type creates fibers for input curves/edges, while the face follower type creates line followers following the input faces.

VSCLs with AFP processes imposes strict limitations on the maximum curvature [3–5]. This is because the process simultaneously layers a large number of independent tows, which necessitates limiting the fiber steering to reduce the occurrence of defects. On the other hand, CF4 processes that utilize a dual extruder mechanism [6,7] — one for heating and depositing the matrix (e.g., Onyx<sup>®</sup>, a short-fiber-reinforced nylon) and the other for depositing the continuous fiber fused filament (CFFF) — extrude a continuous prepreg tow that can accommodate small radii of curvature and sharp changes in fiber direction while retaining fiber continuity throughout the printing process, as illustrated in Fig. 1.

VSCLs are defined as an assembly of layers (also called plies or laminae) with different fiber orientations that are tailored to attain the required mechanical properties, e.g., to maximize the stiffness-to-weight ratio. The fiber orientation in each layer, the layers' thickness, and the stacking sequence — i.e., the order in which individual laminae are placed on top of one another — determine the overall VSCLs' mechanical response. At the same time, it is necessary to satisfy manufacturing constraints imposed by the fabrication process. For example, conventional manufacturing techniques allow layers only with rectilinear fiber reinforcement in the laminate. A common choice is quasi-isotropic orientations ( $0^\circ$ ,  $\pm 45^\circ$ ,  $90^\circ$ ), which mitigates the effects of membrane-bending, membrane-shearing, and bending-shearing coupling responses. In contrast, advanced automated manufacturing techniques like AFP and CF4 can produce layers with variable-fiber reinforcement to tailor the laminate's stiffness (or flexibility), which can also reduce material and manufacturing costs. AFP, however, imposes strict limitations on steering the prepreg tows and/or a maximum ply drop [8], while for CF4 processes ensuring fiber continuity in each layer requires restrictions on the smallest feature size that can be reinforced [9]. Despite the increased flexibility in the fiber reinforcement, obtaining autoclave-level mechanical properties for VSCL fabricated via CF4 is challenging. Studies have reported that the comparatively high void content (10%–12%) and poor interfaces severely affect the mechanical performance of printed CFRP parts [10,11]. Therefore, to obtain the best possible performance of components manufactured by CF4, it is necessary to formulate computational design techniques tailored to the design freedom and manufacturing constraints of this process; this is the focus of the present work.

Compared to designing composite laminates that are made of several straight-fiber plies [12], optimizing variable stiffness composite laminates is challenging since the arrangement of fiber orientation and the thickness of the fiber can all vary throughout the composite laminate [13]. Consequently, VSCLs are analyzed using discretization techniques — e.g., the finite element method (FEM) — assuming a constant fiber orientation within each finite element. As a result, optimizing VSCLs cannot escape the inordinately large number of design variables. Therefore, exploring the vast design space of additively manufactured VSCLs mandates a systematic approach, for which computational design tools have proven to be effective [14]. One such procedure is topology optimization (TO), which can also assist in leveraging CF4's manufacturing capabilities.

Topology optimization is an iterative design procedure that is used to find an optimized distribution of material in a given design domain by minimizing a quantifiable objective function subject to constraints [15–19]. When optimizing VSCLs using the TO approach, a material orientation parameterization is formulated to obtain an optimized distribution of fiber orientations within the design domain. In this context, the choice of parameterization — i.e., the representation of material orientation in the design space — plays a key role in the optimization. Several parameterization schemes have been proposed in the literature [20]: The continuous fiber orientation (CFO) approach [21–25] naturally becomes a suitable parameterization scheme for CF4 processes because it optimizes for continuous orientations in the range  $[-\pi, \pi]$  at each design point, thus providing the highest freedom for designing VSCLs. Curvilinear parameterization schemes represent the fiber path along the principal stress direction, thereby yielding designs with fewer variables than those obtained with elemental fiber angles, all while ensuring that the fiber path continuity is maintained [26–28]. As an alternative to continuous parameterization approaches, discrete material orientation (DMO) methods optimize for a set of discrete fiber orientations using gradient-based optimizers [29]. DMO has been investigated for multi-layer composite laminate designs [30–34] as it can realize practical designs by accommodating restrictions that conform to design guidelines for better structural integrity [35]. Subsequent works combine aspects of CFO and DMO to reduce the risk of falling into local optima without sacrificing fiber continuity [36–39].

Density-based TO methods — e.g., the solid orthotropic material with penalization — are adopted mainly for CFRP materials [40]. These procedures enable the optimization of both the material distribution and the fiber orientation, either simultaneously or sequentially. Density-based TO has a straightforward computer implementation and has proven effective in solving a wide range of problems with coupled differential equations (which we loosely refer to as multiphysics) [41]. However, when designing for CF4 [42–45], the designer must identify standard geometric features from the attained topology (e.g., based on computer-aided-design (CAD) representations) to avoid manufacturing defects and/or unfeasible geometries for the printing process [46]. In addition, these methods yield free-form designs that need to be further post-processed before fabrication through shape and size optimization until the structure satisfies the manufacturing constraints—to the detriment of the mechanical performance of the optimized design. Instead of parameterizing material orientations at the finite element level and then enforcing fiber continuity constraints, an alternative approach can use geometric primitives to represent the fibers and thus ensure manufacturability while simultaneously decoupling the material orientations' space from the finite element discretization; this way, the primitives' geometric parameters become the design variables for the TO problem. These feature mapping TO methods [47] become attractive in these cases, mainly when dealing with anisotropic materials, as pursued in this work.

One feature-mapping TO method that decouples the finite element discretization used for analysis from the design's geometric features is the geometry projection (GP) method [48]. GP uses geometric primitives such as bars and plates endowed with CFRP material properties, which can move freely within the computational design domain. These primitives, which are described by a few design parameters (e.g., the radius of the primitives and the coordinates of the endpoints of its medial axis), are mapped onto a density field that is subsequently discretized by the finite element mesh for analysis. Because this mapping is differentiable, design sensitivities can thus be computed via the chain rule to update the design parameters. By allowing a dual representation of geometric primitives (geometric parameters/densities) and decoupling the design representation from the finite element mesh, GP provides a trade-off between the conventional component-wise assembly of engineering features and the free-form design of CFRP structures, which is advantageous for applications that benefit from this geometric restriction.

GP has been successfully used to optimize the layout of FRBs for maximum structural stiffness [49], both in 2D and 3D, and the technique was later advanced to consider primitives made of fiber-reinforced plates [50,51]. However, GP has mainly been used to design structures as assemblies of individual fiber-reinforced components, and thus, its applicability in designing monolithic composite structures is yet to be demonstrated [52]. A GP technique that produces a design that adheres to the CF4 processes requires capturing the composite stiffness of fiber-reinforced components that form out-of-plane overlaps (or stacks). Subsequently, this can yield bar intersections in the design, which is crucial in lowering the strain energy because the intersection of fibers optimizes the orthotropic ratio ( $E_2/E_1$ ) such that the stiff fiber direction aligns with all the intersecting load paths. This presents a challenge with the current GP methodology because the softargmax function implementation pushes the design to attain a discrete component choice instead of aligning the primitives with all intersecting load paths. That is, in current GP techniques, points that lie at the intersection of two or more primitives (i.e., joints) are assigned the material of one of the primitives, which means they do not capture the mechanical behavior at joints that would be obtained from overlapping components.

In this paper, we build upon the work of Smith and Norato [49] and formulate a novel GP technique to enable the design of VSCLs. While using FRBs as features, we extend GP methods in several important aspects. First, by employing theories that describe composite laminates [53], we endow the GP with the ability to model overlapping FRBs in the design, thus allowing stacking unidirectional plies or lamina. These overlapping regions are then represented in the density field by exploiting the dual nature of GP. Specifically, the equivalent single-layer model based on first-order shear deformation theory is used to compute the laminate stiffness matrices, which also allows the consideration of out-of-plane and/or in-plane loading. Second, we formulate a simple material interpolation approach, which considers the effect of overlapping FRBs by summing the contribution of bars' elasticity tensors. Importantly, when computing the bending stiffness  $D_{Be}$  of the laminate, we assume that all the layers are located at the same distance from the bending axis to be consistent with a simple sum material interpolation; in doing so, the contribution of the stacking sequence to the bending stiffness is neglected. Despite the assumption, capturing the mechanical behavior of overlapping FRBs based on composite laminate theory can help the optimizer in finding a topology with continuously varying and intersecting fiber trajectories, thereby producing a design that accommodates the design freedom offered by CF4 processes. Finally, to ensure that the proposed method yields print-ready designs, we impose a minimum length limit on the bars by using a penalization technique that assigns a length-dependent weight to each component. This weight becomes zero for bars shorter than the minimum length limit, thus effectively removing the bar from the design. The imposition of the minimum length limit via penalization precludes the need for additional constraints in the optimization problem. As a result of the aforementioned contributions, the proposed method enables the topology optimization of VSCLs made of FRBs, which is not possible with existing techniques.

## 2. The geometry projection

The geometry projection (GP) method is a topology optimization technique that represents the design using geometric components — e.g., 2D flat or 3D cylindrical bars or 3D rectangular plates — that are mapped onto a density field. This field is then discretized using a fixed analysis finite element mesh ( $D \subset \mathbb{R}^2$ ), avoiding the need to re-mesh upon design updates. The GP mapping is differentiable, readily allowing for sensitivity calculations with respect to the geometric parameters so that efficient gradient-based nonlinear programming methods can be employed for the optimization. As the chain rule used to compute sensitivities requires derivatives of the optimization functions with respect to the densities, the technique can benefit from sensitivity formulations already developed for density-based topology optimization approaches. First, and for completeness, we briefly describe the GP method for 2D fiber-reinforced bars (FRBs); we roughly follow the presentation of the GP method given in [54]. The proposed LGP-AM formulation for monolithic structures is subsequently introduced.

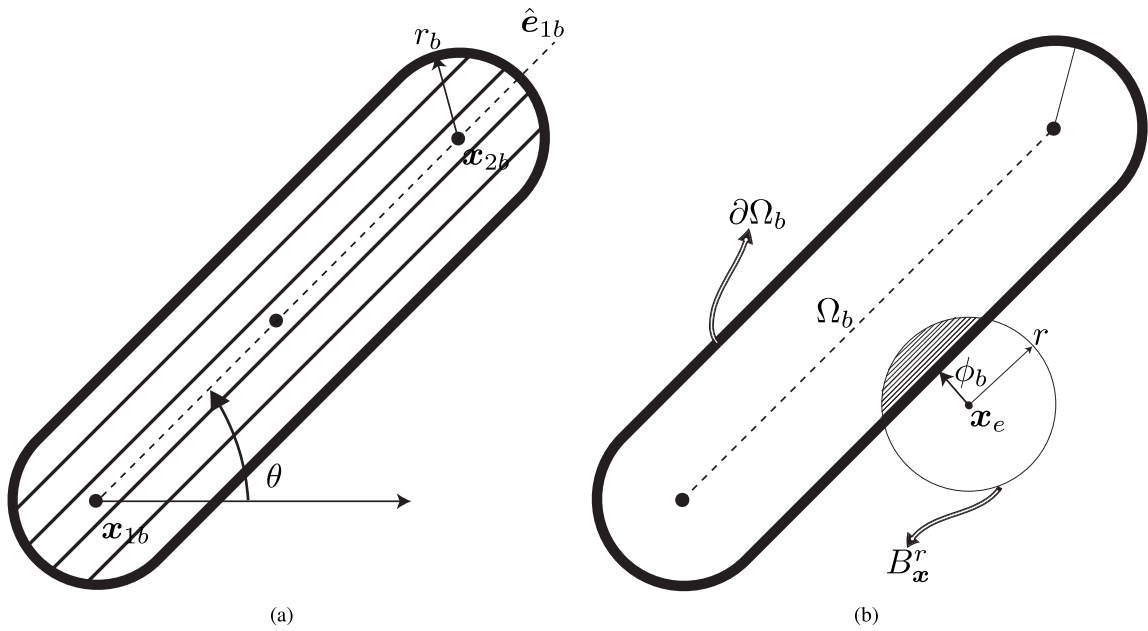


Fig. 2. 2(a) A fiber-reinforced bar with geometric design variables and material orientation. 2(b) Projection of a bar at  $\mathbf{x}$ .

### 2.1. Definition of components and their projected densities

We model a given design by combining multiple FRBs, which form an out-of-plane overlap. The  $b$ th bar  $\Omega_b \in \mathbb{R}^2$  (with  $b$  the index taken from the index set  $\mathcal{B}$  of all bars, i.e.,  $b \in \mathcal{B}$ ), is represented as shown in Fig. 2(a). It is characterized by an offset solid whose medial axis is a line segment, which corresponds to a rectangle with semicircular ends. The bar is completely defined by its two endpoints  $(\mathbf{x}_{1b}, \mathbf{x}_{2b})$ , and a radius  $r_b$  that defines the semicircles and the offset from the medial axis. A membership variable  $\alpha_b \in [0, 1]$  is assigned to each bar and penalized as in density-based methods, which allows the optimizer to remove it from the design or reinsert it. Thus, the  $b$ th bar has design variable vector

$$\mathbf{z}_b = (\mathbf{x}_{1b}, \mathbf{x}_{2b}, r_b, \alpha_b). \tag{1}$$

The GP method maps the design variables of the  $b$ th component onto a component-wise density field  $\rho_b(\mathbf{x}; \mathbf{z}_b)$ , where  $\mathbf{x}$  is the cartesian coordinate in the design region. As illustrated in Fig. 2(b), the projected density at a point  $\mathbf{x}$  is defined as the intersection between  $\Omega_b$  and a ball with radius  $r$  centered at  $\mathbf{x}$ , i.e.,

$$\rho_b(\mathbf{x}; \mathbf{z}_b) = \frac{|B_x^r \cap \Omega_b(\mathbf{z}_b)|}{|B_x^r|}. \tag{2}$$

In 2D, assuming  $r$  is much smaller than the bar's dimensions, then  $\partial\Omega_b$  in  $B_x^r \cap \partial\Omega_b$  can be approximated as a line segment. Therefore, the area fraction of (2) can be computed as the area fraction of the circular segment of height  $h = r - \phi_b$ , where  $\phi_b$  denotes the signed distance from  $\mathbf{x}$  to  $\partial\Omega_b$ . That is, the projected density for bar  $b$  is a single-valued function of  $\phi_b$ , which effectively constitutes a regularized Heaviside function, i.e.,

$$\rho_b(\mathbf{x}; \mathbf{z}_b) = \tilde{H}\left(\frac{\phi_b(\mathbf{x}; \mathbf{z}_b)}{r}\right). \tag{3}$$

The expression for  $\tilde{H}$  is given in Appendix A.2. We follow the convention that the signed distance from points that are inside the bar (i.e.,  $\mathbf{x} \in \Omega_b$ ) is positive, while the signed distance to points outside the bar (i.e.,  $\mathbf{x} \notin \Omega_b$ ) is negative. The signed distance function for a bar is thus the offset minus the distance to the medial line segment, as detailed in the Appendix A.1.

The dual representation — i.e., via geometric parameters or density — can be used to treat individual components as either high-level geometric objects or field variables in component densities. By taking advantage of this dual nature, and as demonstrated in [49], it is possible to incorporate local orthotropic material behavior with a transversely isotropic material response, thus expanding the material design space for designing and optimizing VSCL, as explained later in Section 3.

A penalized density is computed for each bar that is subsequently used to calculate its elastic stiffness tensor using a method similar to the solid-isotropic material with penalization (SIMP) widely used in density-based topology optimization [55]. The penalized density is given by

$$\tilde{\rho}_b^{\text{eff}}(\mathbf{x}; \mathbf{z}_b) = (\alpha_b \rho_b(\mathbf{x}; \mathbf{z}_b))^q, \tag{4}$$

where we recall  $\alpha_b$  is the bar's membership variable, and  $q$  is a penalization parameter. As described below, this penalized density is used to determine the material properties as in SIMP topology optimization techniques. A zero penalized density means the  $b$ th bar does not affect the material properties at  $\mathbf{x}$ . As noted in [54], the membership variable and the projected density must be penalized to ensure that intermediate density regions satisfy the Hashin–Shtrikman bounds.

For the finite element analysis, we assume each finite element has a uniform projected density. As such, the element projected density  $\rho_{be}$  is computed at its centroid  $\mathbf{x}_e$ . The sample window radius  $r$  is fixed and taken to be at least the smallest semi-diagonal of the element.

## 2.2. Combination of components

Section 2.1 describes the geometry projection of a single bar. In previous GP techniques used to design with fiber-reinforced primitives (cf., [49–51]), the intent was to have structures made of individually manufactured fiber-reinforced primitives that are subsequently assembled. In that case, the combination of components is done such that at overlapping regions, only one of the reinforcements of the intersecting bars is selected; in other words, no overlaps of fiber reinforcements were considered. This work, on the other hand, focuses on continuous fiber reinforcement and, therefore, on overlaps where multiple reinforcements are present.

In the GP method of [49], when considering multiple FRBs, the combined element density is defined as a convex combination of each component, i.e.,

$$\check{\rho}_e^{\text{eff}} = \sum_{b=1}^{n_b} w_{be} \check{\rho}_{be}^{\text{eff}} \quad (5)$$

such that  $w_{be} \in [0, 1]$  is the weight for the  $b$ th component, and  $\sum_b w_{be} = 1$ , with  $n_b$  the number of components. These weights thus denote the fractional contribution of each bar to the penalized element density, analogously to the DMO method [29]. The GP method employs the softargmax function as an aggregation function to calculate the weights of overlapping components. The softargmax applies the exponential function to each component density and normalizes these values by dividing by the sum of all these exponentials, as shown in Appendix A.2. The normalization ensures that the sum of the components' weights is 1. As the softargmax parameter  $\beta$  tends to infinity, the softargmax function converges to the argmax function.

This means that the highest penalized effective densities for the intersecting components at a point can be identified, which allows to single out the dominant feature at that point. However, a high value of  $\beta$  results in a highly nonlinear aggregation function, which can cause issues (as discussed in Section 5) when using gradient-based optimizers. Therefore, a finite value of  $\beta = 100$  is typically used (cf. [49]), making the weights  $w_{be}$  approach the discrete one-hot vector that identifies the true maximum. The element elasticity tensors are subsequently calculated by combining the contributions of all elasticity tensors as

$$\mathbf{C}_e = \mathbf{C}_v + \sum_{b=1}^{n_b} w_{be} \check{\rho}_{be}^{\text{eff}} (\mathbf{C}_b - \mathbf{C}_v). \quad (6)$$

The elasticity tensor interpolation  $\mathbf{C}_e$  given by (6) can be used to interpolate between the solid material (bar material  $\mathbf{C}_b$ ) and void material  $\mathbf{C}_v$ .

## 3. Geometry projection formulation for variable-stiffness composite laminates

To enable the topology optimization of VSCLs with FRBs, this work proposes a GP technique based on the following novel ingredients. First, we formulate a material interpolation rule to combine components that accounts for their out-of-plane overlap. Second, a novel length constraint is introduced by modifying the projected density to penalize bars of a length shorter than a specified value  $\underline{\ell}$ . Finally, we formulate an elasticity tensor and, subsequently, element-stiffness matrices based on the proposed material interpolation and on composite laminate theory, that allows for consideration of out-of-plane loads.

### 3.1. Combination of components in proposed LGP-AM method for VSCL

Using (6) to optimize VSCLs may result in a suboptimal solution. This is because this material interpolation does not correctly model the stiffness resulting from the overlap of various reinforced bars. This can significantly impact the design and optimization process for VSCLs, as demonstrated later in Section 5. To circumvent this issue, a straightforward approach is to discard the maximum function approach (which corresponds to a Boolean union of the bars), and compute instead the element's elasticity tensor as the sum of all elasticity tensors:

$$\mathbf{C}_e = \mathbf{C}_v + \sum_{b=1}^{n_b} \check{\rho}_{be}^{\text{eff}} (\mathbf{C}_b - \mathbf{C}_v). \quad (7)$$

Correspondingly, the combined density for the proposed method is given by

$$\check{\rho}_e^{\text{eff}} = \sum_{b=1}^{n_b} \check{\rho}_{be}^{\text{eff}}. \quad (8)$$

This approach was considered for bars made of isotropic materials in [48] and only for in-plane loading. This work considers bars made of an anisotropic material (with the anisotropy endowed by the fiber reinforcement), and it considers out-of-plane loading in addition to in-plane loading. To account for out-of-plane loading, we consider the bending stiffness  $\mathbf{D}_{Be}$  of the laminate, which

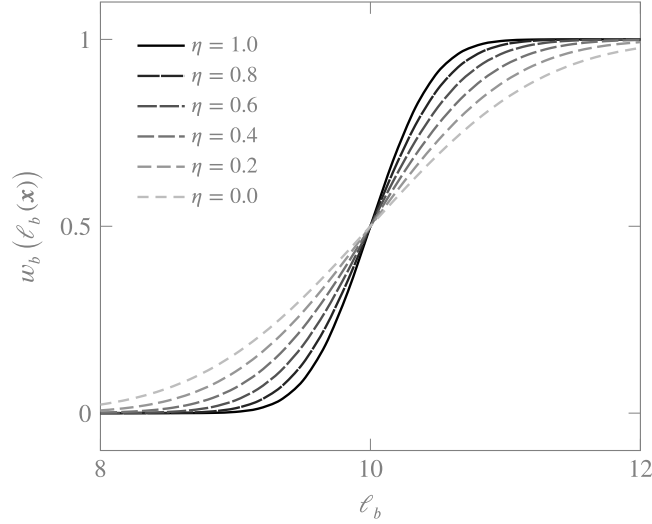


Fig. 3. For  $\underline{\ell} = 10$ —A distribution of length penalty curves are plotted by linearly scaling the steepness parameter,  $\eta$ , from 0 to 1.

is computed by considering the stacking sequence and it is nonlinear [56] (since the moment area of inertia for bending depends nonlinearly on the distance of the laminate relative to the bending neutral axis). The method proposed herein, however, does not account for the stacking sequence. Hence, we assume a uniform contribution of each overlapping feature to the bending stiffness, which is equivalent to assuming all the plies in the laminate lie at the same distance from the bending axis. This assumption is consistent with the simple sum material interpolation of (7).

### 3.2. Minimum length penalization

To ensure the VSCL can be fabricated, it is necessary to prevent components from being too short. To ensure this, we introduce a constraint on the minimum length of each component. Instead of explicitly introducing this requirement as an additional constraint function in the optimization problem, we propose a modification of the projected density  $\rho_{be}^{\text{eff}}$  of the  $b$ th bar, which penalizes the presence of bars with a length less than a specified minimum length  $\underline{\ell}$ . This is achieved by introducing a weight  $w_b \in [0, 1]$ , i.e.,

$$\rho_b^{\text{eff}}(\mathbf{x}; \mathbf{z}_b) = \rho_b(\mathbf{x}; \mathbf{z}_b) \alpha_b w_b(\ell_b(\mathbf{x})). \tag{9}$$

Correspondingly, the penalized density of Eq. (4) becomes

$$\tilde{\rho}_b^{\text{eff}}(\mathbf{x}; \mathbf{z}_b) = (\rho_b(\mathbf{x}; \mathbf{z}_b) \alpha_b w_b(\ell_b(\mathbf{x})))^q. \tag{10}$$

The weight  $w_b$  is calculated using the sigmoid function, given by

$$w_b(\ell_b(\mathbf{x})) := \frac{1}{2} \left[ 1 + \operatorname{erf} \left( \frac{k(\ell_b - \underline{\ell})}{\sqrt{2}} \right) \right], \tag{11}$$

where erf is the error function (see Appendix A.2), and  $\ell_b = \|\mathbf{x}_{2b} - \mathbf{x}_{1b}\| \equiv \|\mathbf{v}_b\|$  is the length of the medial axis vector (see Appendix A.1). The constant  $k = \exp(\eta)$ , with  $\eta \in [0, 1]$ , defines the steepness of the sigmoid curve, as shown in Fig. 3. When the length of the bar  $\ell_b$  is less than the minimum  $\underline{\ell}$ , the weight  $w_b$  approaches zero. As with the membership variable, this means the bar will have no stiffness and it is effectively removed from the design.

### 3.3. Assumptions on overlapping components

Consider a bar  $\Omega_b$  that overlaps with other bars  $\{\Omega_i\}_{i \in B \setminus \{b\}}$ . In the proposed method, a bar corresponds to a ply; therefore, these terms are used interchangeably. The stack of bars forming the overlapping region can be modeled using composite laminate theories. For manufacturing via CF4, a uniform thickness  $H$  is assigned to all FRBs in the stack. We consider the composite laminate formed by the superposition of the bars to have a symmetrical stack up. The symmetry assumption is advantageous as it eliminates the membrane-bending coupling matrix  $\mathbf{D}_{MB}$  and minimizes the wrapping of the printed laminate; thus, only  $n_b$  plies (i.e., bars in the optimization) are modeled.

When considering the position of a ply in the stack, each ply  $b$  is defined by the planes  $z = h_b$  and  $z = h_{b+1}$ , with  $h_b \leq z \leq h_{b+1}$  and  $h_{b+1} - h_b = H$ . The proposed method, however, simplifies the stacking sequence by disregarding it. Therefore, the effect on the

out-of-plane bending stiffness is not considered due to the position in the stack. Expressly, we assume  $h_b = 0$  for all plies. While this assumption introduces some inaccuracy in modeling the out-of-plane stiffness of the laminate, it renders a lower stiffness and, therefore, leads to a conservative design.

It is assumed the laminate satisfies plane-stress conditions. We also make the assumptions of first-order shear deformation theory (FSDT) to model the mechanical behavior of VSCLs. Other hypotheses have been considered to model composite laminates, as discussed elsewhere [53,57]. With FSDT, classical laminate theory [58] is relaxed by considering that the transverse normal does not remain perpendicular to the mid-plane ( $z = 0$ ) after deformation; this implies the theory assumes a linear variation of the in-plane displacements through the thickness, which results in constant transverse shear strain. This involves incorporating the transverse shear strain into the theory, which allows the extension of the elastic displacement in the FSDT to take the following form:

$$\begin{aligned} u(x, y, z) &= u_0(x, y) + z\psi_{0x}(x, y), \\ v(x, y, z) &= v_0(x, y) + z\psi_{0y}(x, y), \\ w(x, y, z) &= w_0(x, y), \end{aligned} \quad (12)$$

where  $u_0, v_0, w_0$  correspond to the displacements of the laminate's mid-plane, and  $\psi_{0x}$  and  $\psi_{0y}$  the rotations of the normals to the mid-plane about the  $y$ - and  $x$ -axis, respectively. The proposed method assumes that the continuous displacement field between the plies satisfies Eq. (12).

### 3.4. Bar elasticity tensor

The material coordinate system (MCS) of a bar, shown in Fig. 2(a), is denoted by  $\{\hat{e}_{1b}, \hat{e}_{2b}, \hat{e}_{3b}\}$ , and the laminate coordinate system (LCS) is denoted by  $\{e_1, e_2, e_3\}$ . It is assumed the fiber reinforcement is aligned with  $\hat{e}_{1b}$ ; and  $\hat{e}_{2b}$  is defined so that it is perpendicular to  $\hat{e}_{1b}$ , and so that  $e_3 = \hat{e}_{1b} \times \hat{e}_{2b}$  corresponds to the global out-of-plane axis, leaving the page in Fig. 2(a). The components of the coordinate transformation matrix between these coordinate systems can be obtained from the direction cosines  $R_{ij}^b = e_i \cdot \hat{e}_{jb}$ . The components of the elasticity tensor  $C_b$  of bar  $b$  in LCS are given by

$$(C_b)_{ijkl} = \sum_{p,q,r,s} R_{ip}^b R_{jq}^b R_{kr}^b R_{ls}^b (\hat{C}_b)_{pqrs}, \quad (13)$$

where  $\hat{C}_b$  is the elasticity tensor in MCS. For plane stress of the laminate, this transformation reduces to

$$C_b^p = T_1^T \hat{C}_b^p T_1 \quad \text{and} \quad C_b^s = T_2^T \hat{C}_b^s T_2, \quad (14)$$

with

$$T_1 = \begin{bmatrix} c^2 & s^2 & cs \\ s^2 & c^2 & -cs \\ -2cs & 2cs & c^2 - s^2 \end{bmatrix}, \quad T_2 = \begin{bmatrix} c & -s \\ s & c \end{bmatrix}, \quad (15)$$

where  $c = \cos \theta, s = \sin \theta$ , and  $\theta$  is the angle between the axes  $\hat{e}_1$  and  $x$ , as shown in Fig. 2(a). The  $3 \times 3$  matrix  $\hat{C}_b^p$  relates the in-plane strains  $\{\epsilon_x, \epsilon_y, \gamma_{xy}\}$  to the stresses  $\{\sigma_x, \sigma_y, \tau_{xy}\}$  in LCS; similarly, the  $2 \times 2$  matrix  $\hat{C}_b^s$  relates the out-of-plane shear strains  $\{\gamma_{xz}, \gamma_{yz}\}$  to the stresses  $\{\tau_{xz}, \tau_{yz}\}$  in LCS.

### 3.5. Laminate elasticity matrix

Using the material interpolation (7), the effective laminate elasticity tensor is given by

$$D = C_v + \sum_{b=1}^{n_b} \rho_{be}^{\text{eff}} (D_{0b} - C_v), \quad (16)$$

where

$$D_{0b} = \begin{bmatrix} D_{Mb} & \mathbf{0}_{3 \times 3} & \mathbf{0}_{3 \times 2} \\ \mathbf{0}_{3 \times 3} & D_{Bb} & \mathbf{0}_{3 \times 2} \\ \mathbf{0}_{2 \times 3} & \mathbf{0}_{2 \times 3} & D_{Sb} \end{bmatrix}. \quad (17)$$

In the above,  $D_{Mb}$ ,  $D_{Bb}$ , and  $D_{Sb}$  are the membrane, bending, and shear matrices for bar  $b$ , respectively, given by

$$D_{Mb} = (h_{b+1} - h_b) C_b^p \quad (18)$$

$$D_{Bb} = \frac{1}{3} [h_{b+1}^3 - h_b^3] C_b^p \quad (19)$$

$$D_{Sb} = (h_{b+1} - h_b) \kappa C_b^s, \quad (20)$$

with  $\kappa = 5/6$  the shear correction factor. The off-diagonal blocks of (17) are zero, following the assumption that the laminate has a symmetric stack up, eliminating the membrane-bending coupling matrix  $D_{MBb}$ . Finally, the assumption of uniform ply thickness  $H$  renders  $(h_{b+1} - h_b) = H$  and the assumption that the effect of stacking on the bending stiffness is disregarded (with  $h_b = 0$ ) leads



to  $(h_{b+1}^3 - h_b^3) = H^3$  for all bars. Note that  $D_{0b}$  is design-dependent because the matrices  $C_b^p$  and  $C_b^s$  for bar  $b$  in LCS depend on the orientation  $\theta$  of the bar through the transformation in (14), which in turn depends on the endpoints  $x_{1b}$  and  $x_{2b}$  of the bar's axis.

### 3.6. Element stiffness matrix and FE assembly

Using the laminate elasticity matrix from the previous section, we now construct the element stiffness matrices for the analysis. Without loss of generality, we consider four-node, bilinear, quadrilateral, and plane-stress elements. For brevity, the element stiffness matrix for the  $e$ th element is parameterized by the master coordinate  $(\xi, \eta)$  from the reference canonical element  $\bar{\Omega} = [-1, 1] \times [-1, 1]$ . The bar density  $\rho_b^{\text{eff}}$  is evaluated at the element centroid (i.e.,  $(\xi, \eta) = (0, 0)$ ) and considered uniform within the element. Consequently, the laminate stiffness matrix is also assumed to be uniform in the element.

The displacements and rotations are interpolated within element  $e$  as

$$u_e(\xi, \eta) = \sum_{i=1}^4 N_i(\xi, \eta) a_i^{(e)}, \tag{21}$$

where  $u_e = [u_0 \ v_0 \ w_0 \ \psi_x \ \psi_y]^T$  is the field vector,  $a_i^{(e)} = [u_{0i} \ v_{0i} \ w_{0i} \ \psi_{xi} \ \psi_{yi}]^T$ , its corresponding local degree of freedom vector containing displacements and rotations, and  $N_i(\xi, \eta)$  is a bilinear shape function. Eq. (21) can be expressed in matrix form by defining the shape functions  $N(\xi, \eta)$  as:

$$\begin{bmatrix} N_1 & 0 & 0 & 0 & 0 & \vdots & N_4 & 0 & 0 & 0 & 0 \\ 0 & N_1 & 0 & 0 & 0 & \vdots & \dots & 0 & N_4 & 0 & 0 & 0 \\ 0 & 0 & N_1 & 0 & 0 & \vdots & \vdots & 0 & 0 & N_4 & 0 & 0 \\ 0 & 0 & 0 & N_1 & 0 & \vdots & \dots & 0 & 0 & 0 & N_4 & 0 \\ 0 & 0 & 0 & 0 & N_1 & \vdots & \vdots & 0 & 0 & 0 & 0 & N_4 \end{bmatrix}$$

The element's local stiffness matrix  $k_e$  is finally given by

$$k^{(e)} = \int_{\Omega_e} B^T D^{(e)} B \, d\Omega = \int_{\square} B^T D^{(e)} B j \, d\xi \, d\eta, \tag{22}$$

where the last integral is conducted on the canonical element (denoted by  $\square$ ) using Gaussian quadrature, and thus  $j$  is the Jacobian of the transformation,  $D^{(e)}$  is computed with (17), and the  $B$  matrix — which relates displacements and rotations to strains and curvatures, respectively — for the Q4 element is  $B = [B_1 \ B_2 \ B_3 \ B_4]$ , where for the  $i$ th node

$$B_i = \begin{bmatrix} B_{m_i} \\ B_{b_i} \\ B_{s_i} \end{bmatrix} = \begin{bmatrix} \frac{\partial N_i}{\partial x} & 0 & 0 & 0 & 0 \\ 0 & \frac{\partial N_i}{\partial y} & 0 & 0 & 0 \\ \frac{\partial N_i}{\partial y} & \frac{\partial N_i}{\partial x} & 0 & 0 & 0 \\ 0 & 0 & 0 & -\frac{\partial N_i}{\partial x} & 0 \\ 0 & 0 & 0 & 0 & -\frac{\partial N_i}{\partial y} \\ 0 & 0 & 0 & -\frac{\partial N_i}{\partial y} & -\frac{\partial N_i}{\partial x} \\ 0 & 0 & \frac{\partial N_i}{\partial x} & -N_i & 0 \\ 0 & 0 & \frac{\partial N_i}{\partial y} & 0 & -N_i \end{bmatrix}. \tag{23}$$

Similarly, assuming the absence of body forces, the local force vector is computed as:

$$f_e = \int_{\partial\Omega_e} N^T \bar{t} \, d\Omega = \int_{\partial\square} N^T \bar{t} j \, d\xi, \tag{24}$$

where  $\bar{t}$  is the prescribed traction on the boundary. Note that the local force vector  $f_e$  is computed on the edges of elements that intersect the Neumann boundary.

Lastly, the global stiffness matrix and the global force vector are obtained as:

$$K = \bigtriangleup_{e=1}^N k^{(e)} \quad \text{and} \quad F = \bigtriangleup_{e=1}^N f^{(e)}, \quad \text{respectively,} \tag{25}$$

where,  $\bigtriangleup$  denotes the standard assembly operator,  $N$  is the total number of elements in the discretization. The final system of linear equations that describes equilibrium is then

$$KU = F, \tag{26}$$

where we solve for the global degree of freedom vector  $U$  containing both displacements and rotations.

#### 4. Optimization problem and sensitivity analysis

We consider two optimization problems to demonstrate the proposed approach. The first is the compliance minimization problem subject to a volume fraction, stated as

$$\begin{aligned} \min_{\{z_b\}} \quad & f := \log(c + 1) \\ \text{subject to:} \quad & v \leq \bar{v} \\ & \mathbf{K}\mathbf{U} = \mathbf{F} \\ & z_i \leq z_i \leq \bar{z}_i, \quad i = 1, 2, \dots, n_z, \end{aligned} \quad (27)$$

where  $c = \mathbf{U}^\top \mathbf{F}$  is the compliance,  $[z_i, \bar{z}_i]$  are lower and upper bounds on the  $i$ th design variable,  $\bar{v}$  is a prescribed upper-limit on the volume fraction, and  $v$  is the volume fraction defined as

$$v := \frac{\sum_e v^{(e)}}{\sum_e |\Omega^{(e)}|}. \quad (28)$$

The second problem corresponds to the design of a linear compliant mechanism that maximizes the output displacement at a given point, for which the objective function of Eq. (27) is redefined as:

$$\min_{\{z_b\}} \quad u_o := -\mathbf{L}^\top \mathbf{U}, \quad (29)$$

where  $\mathbf{L}$  is a zero vector except for a unity value at the degree of freedom corresponding to the output port.

In the proposed method, the element volume is calculated as

$$v^{(e)} := |\Omega^{(e)}| \sum_{b=1}^{n_b} \rho_{be}^{\text{eff}}. \quad (30)$$

Importantly, we use the notation  $\rho_{be}^{\text{eff}}$  to denote the evaluation of the penalized density  $\tilde{\rho}_{be}^{\text{eff}}$  of (10) using  $q = 1$ . As known in geometry projection techniques (cf. [48,59]), this is necessary for the penalization of the membership variables to be effective, similar to SIMP methods for density-based methods for topology optimization.

We employ various strategies to promote good convergence of the optimization, cf. [48,49]. First, we employ the log-scaled compliance  $f(\mathbf{z}) = \log(1 + c(\mathbf{z}))$ , which damps large oscillations in compliance when the structure becomes disconnected from the loads or supports. Second, we scale the design variables and impose a uniform move limit  $m$  on the scaled variables at each iteration  $I$  as

$$\begin{aligned} \hat{z}_i &:= \frac{z_i - \bar{z}_i}{\bar{z}_i - z_i} \\ \max(0, z_i^{I-1} - m) &\leq z_i^I \leq \min(1, z_i^{I-1} + m). \end{aligned} \quad (31)$$

Lastly, a continuation technique (as commonly used in topology optimization techniques, cf. [60]) is applied to slowly increase  $\eta$  and therefore the steepness of the error function of (11), which ensures the length penalization does not eliminate components at early optimization iterations.

Due to the cost of the finite element analysis necessary to compute the compliance for a given design, it is desired to employ efficient gradient-based nonlinear programming methods to solve problem (27). This requires computation of the design sensitivities of the objective and constraints in the optimization. The design sensitivity of the penalized effective density of (10) with respect to a design variable  $z_i$  is given by

$$\frac{\partial \rho_b^{\text{eff}}}{\partial z_i} = q (\rho_b^{\text{eff}})^{1-1/q} \left[ \alpha_b \frac{\partial \rho_b}{\partial z_i} w_b + \rho_b \frac{\partial \alpha_b}{\partial z_i} w_b + \rho_b \frac{\partial w_b}{\partial z_i} \alpha_b \right]. \quad (32)$$

We omit a presentation of the derivatives  $\partial \rho_b / \partial z_i$  and  $\partial \alpha_b / \partial z_i$  for brevity as they are provided in prior works, see for example [50]. The derivatives of the length-penalization weights  $w_b$  with respect to the endpoints of the bar's axis can be readily obtained as

$$\frac{\partial w_b}{\partial z_i} = \begin{cases} \frac{\partial w_b}{\partial \ell_b} (\mathbf{x}_{1b} - \mathbf{x}_{2b}) / \ell_b & \text{if } z_i \equiv \mathbf{x}_{1b}, \\ \frac{\partial w_b}{\partial \ell_b} (\mathbf{x}_{2b} - \mathbf{x}_{1b}) / \ell_b & \text{if } z_i \equiv \mathbf{x}_{2b}, \\ 0 & \text{if } z_i \equiv \alpha_b. \end{cases} \quad (33)$$

The term  $\partial w_b / \partial \ell_b$  can be obtained from (11) as

$$\frac{\partial w_b}{\partial \ell_b} = \frac{k}{\sqrt{2\pi}} \exp\left(-\frac{k^2 (\ell_b - \ell_c)^2}{2}\right). \quad (34)$$

Problem (27) is self-adjoint; hence, the sensitivity of the compliance is computed as

$$\partial_{z_i} c = - \sum_e \mathbf{u}^\top \left( \partial_{z_i} \mathbf{k}^{(e)} \right) \mathbf{u}. \quad (35)$$

The derivative of the objective function is  $\partial_{z_i} f = 1/(1 + \partial_{z_i} c)$ . The term  $\partial_{z_i} \mathbf{k}^{(e)}$  is obtained by differentiating (22):

$$\partial_{z_i} \mathbf{k}^{(e)} = \int_{\Omega^{(e)}} \mathbf{B}^\top \partial_{z_i} \mathbf{D}^{(e)} \mathbf{B} \, d\Omega^{(e)}; \quad (36)$$

**Table 1**  
Material properties used for all the examples.

Material	$E_1$ [GPa]	$E_2$ [GPa]	$\nu_{12}$	$G_{12}$ [GPa]	$G_{13}$ [GPa]	$G_{23}$ [GPa]
Carbon epoxy AS4/3501-6	113.6	9.650	0.334	6.0	6.0	3.1

and from (16), we obtain

$$\partial_{z_i} \mathbf{D}^{(e)} = \sum_{b=1}^{n_b} \left[ \frac{\partial \rho_{be}^{\text{eff}}}{\partial z_i} (\mathbf{D}_{0b} - \mathbf{C}_v) + \rho_{be}^{\text{eff}} (\partial_{z_i} \mathbf{D}_{0b}) \right]. \tag{37}$$

As noted in Section 3.5,  $\mathbf{D}_{0b}$  depends on the positions of the endpoints of the bar’s axis. The derivative of the transformation in (14) is straightforward to obtain but omitted here for brevity; the reader is referred to [49] for details.

Similarly, for the compliant mechanism problem (29), the derivative of the output displacement is obtained from Eq. (36) as

$$\frac{\partial u_o}{\partial z_i} = \lambda^\top \partial_{z_i} \mathbf{k}^{(e)} \mathbf{u}, \tag{38}$$

where  $\lambda$  is the solution to the adjoint load problem  $\mathbf{K}\lambda = \mathbf{L}$ .

The derivative of the volume constraint is simply given by

$$\partial_{z_i} v = \frac{1}{\sum_e |\Omega^{(e)}|} \left( \sum_e |\Omega^{(e)}| \sum_{b=1}^{n_b} \frac{\partial_{z_i} \rho_{be}^{\text{eff}}}{\partial z_i} \right), \tag{39}$$

where  $\partial_{z_i} \rho_{be}^{\text{eff}} / \partial z_i$  can be obtained from (32) with  $q = 1$ .

### 5. Examples

The method outlined in this paper is demonstrated with four numerical examples, shown in Fig. 4. All examples consider bars made of CCFRP with fiber reinforcement aligned with the bar’s axis. Table 1 lists the corresponding material properties. The first four examples consider the compliance minimization problem, and the last example corresponds to a compliant mechanism design problem.

The following settings are considered for all the examples unless otherwise noted. The method-of-moving-asymptotes (MMA) [61] is employed for the optimization, with the default parameters described in [62], i.e.,  $a_0 = 1$  for the objective function, and  $a_i = 0, c_i = 1000$  and  $d_i = 1$  for every constraint  $i$  in the optimization. The void material is isotropic with Young’s modulus  $E^{\text{void}} = 10^{-3} E_1$  and Poisson’s ratio  $\nu^{\text{void}} = 0.3$ . The radius of the bars in the initial design is the midpoint of the radius bounds. The initial values of the membership variables are all set to  $\alpha = 0.5$ . The move limit on the scaled design variables is  $m = 0.02$ . Finally, the steepness parameter  $\eta$  for the length constraint is increased at each iteration from 0 to 1 with a step of 0.025.

The optimization is stopped based on the satisfaction of any of the three conditions. The first condition is met when the 2-norm of the change in the design variable vector is less than 0.002. The second criterion is reached when the Karush-Kuhn–Tucker (KKT) condition norm is less than 0.002. The third criterion is satisfied when the change in the objective function in consecutive iterations is less than  $10^{-9}$ . Finally, the optimization is stopped at 450 iterations if the foregoing criteria are not satisfied.

The projected densities of the bars in the plots corresponding to the GP method are shown in the same way as in [49], namely, colors for each orientation are determined by the color wheel shown in Fig. 5. Since, in that method, there are no out-of-plane bar overlaps, this coloring scheme is useful to identify which reinforcement orientation has been assigned by the optimizer in regions where bars intersect. This type of distinction is unnecessary for the method proposed here since bars overlap out-of-plane at intersections. For a similar reason, transparency is used in the color of the bars for the LGP-AM designs to help distinguish overlapping components. It should be noted that, when comparing the results produced by the proposed method to those of the GP method, we are specifically referring to the GP method of [49].

#### 5.1. MBB beam

The first example considers a simply supported beam in 3-point bending of dimensions 300 mm × 50 mm. This is a well-known benchmark in topology optimization for minimal compliance, referred to as the (Messerschmitt–Bölkow–Blohm) MBB beam. The volume fraction limit is set to 0.5. Since the problem is symmetric, only one-half of the design region is modeled, and symmetry boundary conditions are used for the analysis, as depicted in Fig. 4. A 1 kN load is applied at the beam’s midpoint. The initial design consists of 27 bars, and the design variables have the following bounds:

$$\left\{ \begin{matrix} (0, 0) \\ 2 \\ 0 \end{matrix} \right\} \leq \left\{ \begin{matrix} (\mathbf{x}_{b1}, \mathbf{x}_{b2}) \\ r_b \\ \alpha_b \end{matrix} \right\} \leq \left\{ \begin{matrix} (150, 50) \\ 5 \\ 1 \end{matrix} \right\}. \tag{40}$$

In this particular scenario, in which a single load is applied, it is known that the minimum-compliance structure made of elastic, heterogeneous orthotropic materials is one for which the load members are aligned with the principal stress directions at each

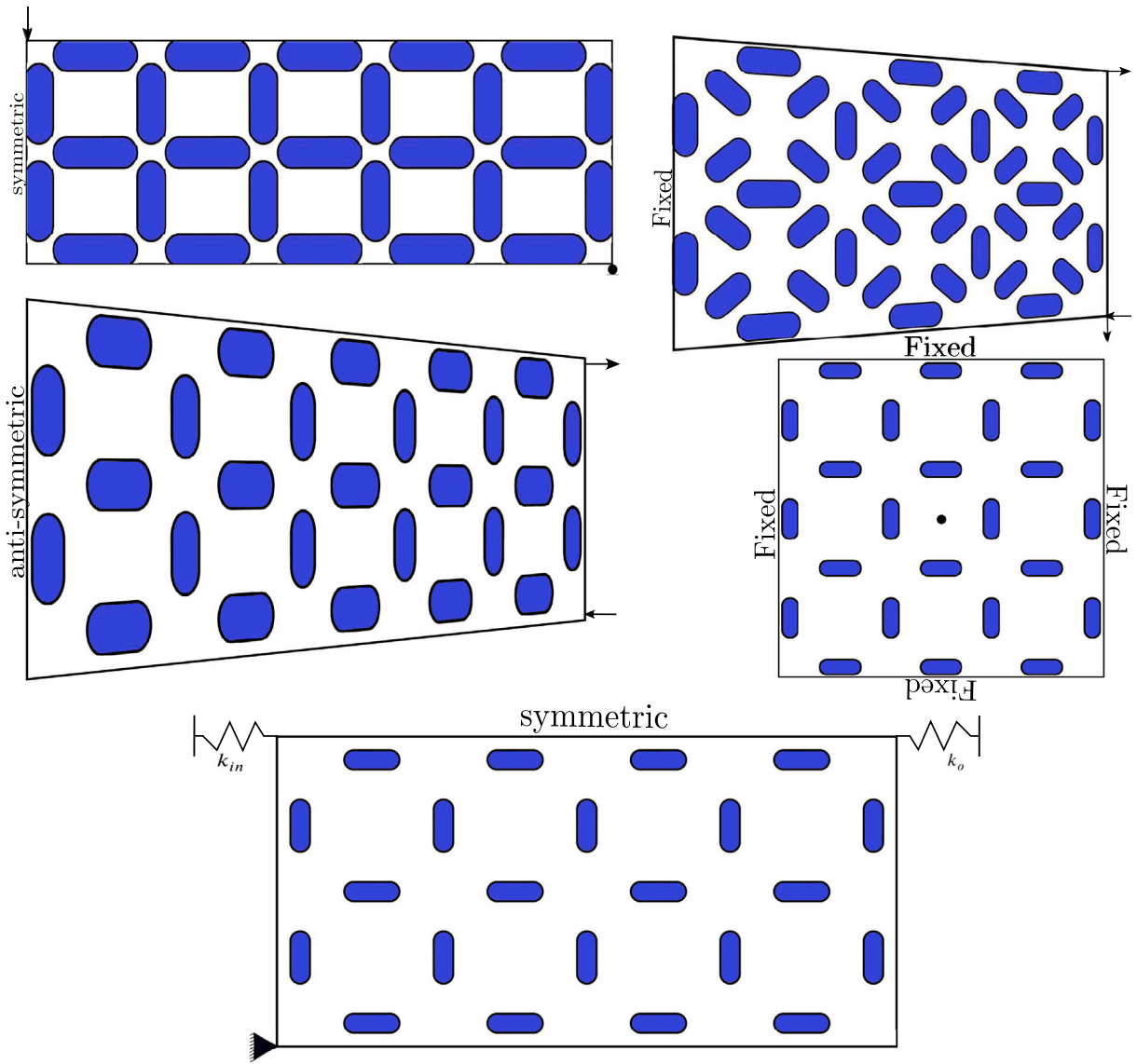


Fig. 4. Design region, boundary conditions, and initial design, for example, problems: beam in 3-point in-plane bending (top left); rectangular plate in pure torsion (middle left); cantilever beam under in- and out-of-plane bending (top right); square membrane in out-of-plane bending (middle right) and single input-output complaint mechanism.

point in the design [63]. Moreover, as this result also applies to structures made of isotropic materials, we expect the result of the proposed method to obtain similar designs to well-known Michell-type solutions for the MBB beam.

Table 2 shows the optimal designs obtained with the GP and the proposed method with and without a minimum length constraint. While both methods produce designs that are reminiscent of well-known Michell-type solutions for the MBB beam, the GP method design appears to produce a ‘bulkier’ design. This occurs because no overlaps are allowed in the GP method of [49]; therefore, to increase the stiffness of the beam, the optimizer makes the bars wider. In the LGP-AM method, on the other hand, the optimizer can increase the stiffness by ‘piling up’ bars in the out-of-plane direction. In other words, while the GP method only increases the stiffness by adding material in the plane, the LGP-AM method can add material in and out of the plane. For the same reason, the LGP-AM designs appear more slender, although all designs have the same amount of material. Also, for the same reason, the LGP-AM designs are stiffer because the overlap of bars (particularly along the top and bottom edges of the beam) can render a larger second-moment area of inertia and, consequently, higher bending stiffness for the same amount of material. That is, the increase in width of bars made by the GP method in bars along, e.g., the bottom edge of the beam is akin to increasing the thickness of the flange of an I-beam, whereas the overlapping of bars in the LGP-AM method is akin to increasing the width of the flange (cf. [48]). For an equal-volume increase, the latter will render a higher bending stiffness. The LGP-AM design with no minimum length constraint

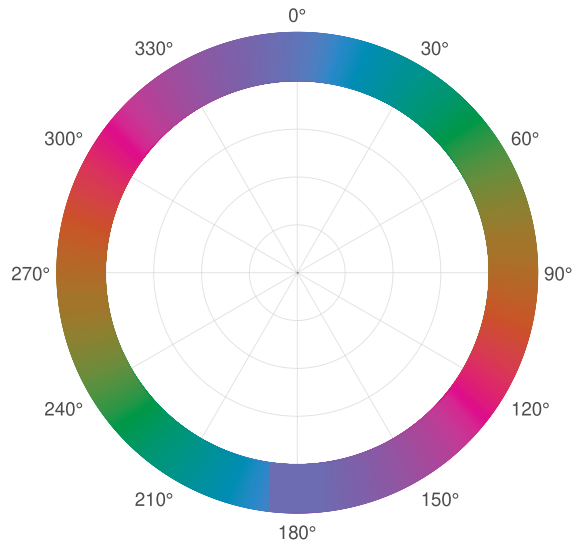


Fig. 5. Color wheel used for combined density plots corresponding to designs obtained with the GP method. The color indicates the orientation of the primitive. (For interpretation of the references to color in this figure legend, the reader is referred to the web version of this article.)

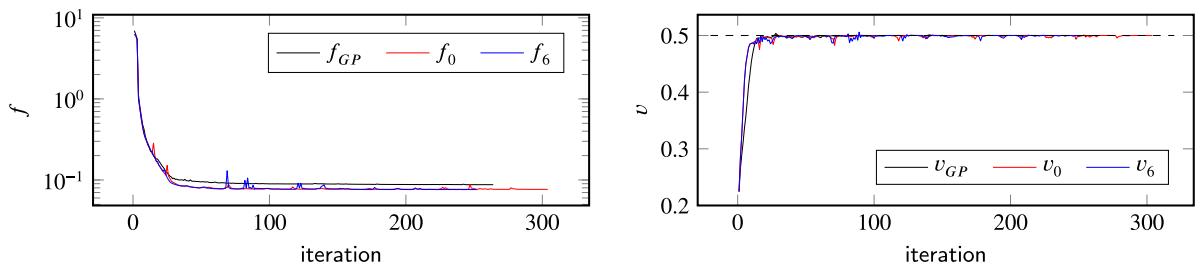


Fig. 6. Objective (left) and volume constraint (right) histories for the MBB beam designs of Table 2 corresponding to the GP design ( $f_{GP}$  and  $v_{GP}$ ), and the LGP-AM designs with no minimum length constraint ( $f_0$  and  $v_0$ ) and with a 6 mm minimum length constraint ( $f_6$  and  $v_6$ ).

(i.e., with  $\underline{\ell} = 0$  mm) renders a short bar with  $\ell = 3.4734$  mm (highlighted in Table 2 with a thicker boundary). However, the design attained with the minimum length constraint  $\underline{\ell} = 6$  mm does not produce short bars. The plot in Fig. 6 shows that the optimization process exhibits a typical behavior for compliance minimization, namely with a significant decrease in the first few iterations, followed by smaller adjustments to the design variables in subsequent iterations. In the case of LGP-AM with a length constraint, some jumps occur when features with lengths below  $\underline{\ell}$  are removed, occasionally resulting in a disconnected structure with increased compliance. A pronounced peak indicates the removal of components near the load application or disconnected structure, while less intense peaks correspond to the removal of bars for which the structure remains connected. Despite the occurrence of these jumps during optimization, the LGP-AM converges smoothly in the later stages, demonstrating the method’s effectiveness. It is important to note that, as discussed in [47], feature-mapping techniques like the GP method are more dependent on the initial design than, e.g., density-based and level-set techniques. Nevertheless, as shown by the designs in Table 2, the optimizer has no problem finding good designs that resemble well-known optimal solutions from the arbitrarily selected initial designs.

### 5.2. Rectangular plate under torsion

The second example considers a rectangular plate of dimensions 350 mm×50 mm under out-of-plane torsion, as depicted in Fig. 4. Using anti-symmetry conditions and assuming a symmetric design, the FE analysis and the optimization are performed on half of the plate. The design region is discretized using  $175 \times 50$  bilinear, quadrilateral elements. The midpoint of the left-hand side edge is fixed to restrict rigid motion. Concentrated, out-of-plane loads are applied at the right edge’s vertices, producing an equivalent

**Table 2**

Optimal designs and combined density for the MBB beam. The color of the bars for the optimal designs in the third column corresponds to their penalized membership variable value  $\alpha_b^q$ , and the bars are plotted with transparency to facilitate the visualization of all bars. In the last column, the density plots for the GP (top row) and LGP-AM (second and third row) methods correspond to the combined densities of Eqs. (5) and (8), respectively.

$\underline{\ell}$ (mm)	$c$ (kN mm)	Design	Combined density
-	1.038		
0	0.905		
6	0.898		

torque of 50 kNmm. Away from the point of application of the loads, by Saint-Venant’s principle, the plate is under pure torsion. The initial design consists of 29 bars (see Fig. 4), and the bounds imposed on the design variables are as follows:

$$\begin{Bmatrix} (0, 0) \\ 2 \\ 0 \end{Bmatrix} \leq \begin{Bmatrix} (\mathbf{x}_{b1}, \mathbf{x}_{b2}) \\ r_b \\ \alpha_b \end{Bmatrix} \leq \begin{Bmatrix} (175, 50) \\ 5 \\ 1 \end{Bmatrix}. \tag{41}$$

We consider four cases for this example: two volume fraction limits of  $\bar{v} = 0.4$  and  $\bar{v} = 0.5$ , each without a minimum length constraint and with a length constraint  $\underline{\ell} = 6$  mm. Table 3 shows the optimization result with the proposed LGP-AM and GP methods. In all the LGP-AM cases, the optimal designs generally exhibit bars at angles of  $\approx \pm 45^\circ$  relative to the plate axes, with bar intersections located along the plate axes. This is expected since the plate is subjected to torsion, which leads to most of the plate being under pure shear, and consequently, the maximum shear stresses occur at  $\pm 45^\circ$ . Consequently, and since the reinforcement of the bars is along the bar’s axis, we expect the bars to be aligned with these directions to minimize compliance. Also, the pure-torsion state means the in-plane ( $D_{M33}$  and  $D_{B33}$ ) and out-of-plane torsional stiffness  $D_S$  components of the laminate are the main contributors to minimizing the plate’s compliance. The first row of Table 3 shows the design obtained for  $\bar{v} = 0.4$  with no minimum length constraint. This design exhibits some short bars that cannot be manufactured and some disconnected bars. Also, the optimization reaches the maximum number of iterations, as shown in Fig. 7. When the length constraint is introduced, as shown in the second row of Table 3, the design no longer exhibits short bars and is fully connected. The optimization exhibits better convergence (it satisfies the stopping criteria in 350 iterations, as shown in Fig. 7), and the compliance is noticeably lower than in the previous case, likely due to the disconnected features in the design without length constraint. The third and fourth rows of Table 3 correspond to the designs with  $\bar{v} = 0.5$  and with  $\underline{\ell} = 0$  mm and  $\underline{\ell} = 6$  mm, respectively. The topology of the designs with  $\bar{v} = 0.5$  and  $\bar{v} = 0.4$  is similar, however the former has more short bars, primarily located on the overlaps. The introduction of the length constraint for the design with  $\bar{v} = 0.5$  eliminates the short bars and, interestingly, produces a design with a similar compliance value to the one with no length constraint. This means the length constraint in this example does not impose a penalty on compliance and leads the optimization to a better design in terms of manufacturability. Moreover, when comparing the LGP-AM designs with the GP design, it is observed that the GP method converges to a suboptimal design. Unlike the LGP-AM method, in which overlaps can have reinforcement in multiple directions (in the case of this example,  $\pm 45^\circ$ ), the GP method enforces a single reinforcement orientation at every point in the structure via the softargmax maximum approximation. It is possible that this leads the optimizer to converge to a poor local minimum in the GP method. This example demonstrates that the proposed LGP-AM method is better suited than the GP method to design VSCLs.

Finally, we consider an optimized design with a volume fraction of 40% and a minimum length constraint of 6 mm obtained with the LGP-AM method. This design can be seamlessly printed using the CF4 process from 9tlabs [6]. Fig. 8 shows a solid-model interpretation of the symmetric optimized design created using CAD software (SolidWorks® 2024, Dassault Systèmes). The solid model is then exported as a stereolithography file (STL) and imported into the 9tlabs’ slicing software, Fibrify®, to create fiber trajectories using a “line follower” fill type.

**Table 3**  
Optimal designs and combined density for a plate under out-of-plane torsion load. Rows 1–4: LGP-AM designs. Last row: GP design.

$\ell$ (mm)	$\bar{v}$	$c$ (kN mm)	Design	Combined density
0	0.4	147.37		
6	0.4	129.99		
0	0.5	105.15		
6	0.5	104.21		
-	0.5	126.44		

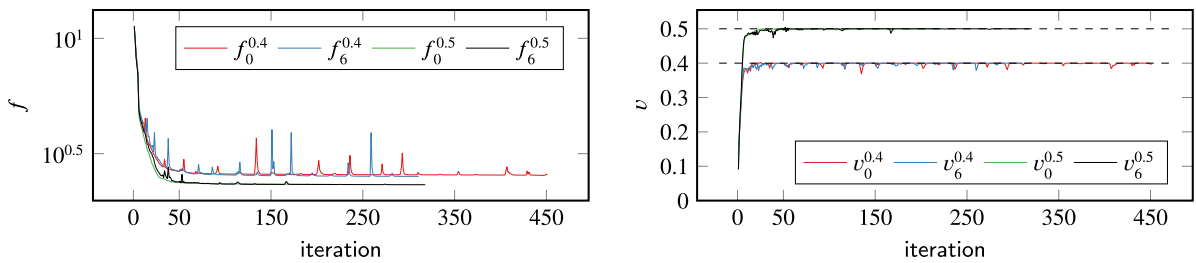


Fig. 7. Objective (left) and volume constraint (right) histories for the designs shown in Table 3 correspond to the LGP-AM designs. The subscripts and superscripts in the curve labels indicate the minimum length constraint and volume fraction limits, respectively.

### 5.3. Square plate under out-of-plane point load

The third example considers a fixed square plate of dimensions of 150 mm × 150 mm under an out-of-plane concentrated load of 50 kN applied at the center of the square plate, as shown in Fig. 4. The design region is discretized using 150 × 150 bilinear, quadrilateral elements. Although the analysis problem has two planes of symmetry, we consider the entire design region to determine the extent to which the optimization produces a symmetric design. The design is initialized with 24 bars, and the bounds imposed on the design variables are as follows:

$$\begin{Bmatrix} (0, 0) \\ 3 \\ 0 \end{Bmatrix} \leq \begin{Bmatrix} (\mathbf{x}_{b1}, \mathbf{x}_{b2}) \\ r_b \\ \alpha_b \end{Bmatrix} \leq \begin{Bmatrix} (150, 150) \\ 6 \\ 1 \end{Bmatrix} \tag{42}$$

The expected optimal solution for this problem consists of a cross shape connected to the midpoints of the sides of the design region, as has been demonstrated both for isotropic (Pedersen) and short fiber-reinforced [65] materials. The optimization is performed with the proposed LGP-AM method with minimum length constraints of  $\ell = 0$  mm and  $\ell = 12$  mm.

Table 4 shows the designs with and without the minimum length constraint. As expected, the optimization produces a cross-shaped design. However, the design is slightly asymmetric. This is not unexpected since it is known that the more restrictive design representation imposed by the bars, which employs far fewer variables than density-based and level-set methods, may lead to an optimal design that is asymmetric. This is consistent with similar findings for topology optimization of truss structures. To understand why this occurs, consider a symmetric design whose volume fraction is slightly below or above the volume fraction constraint and

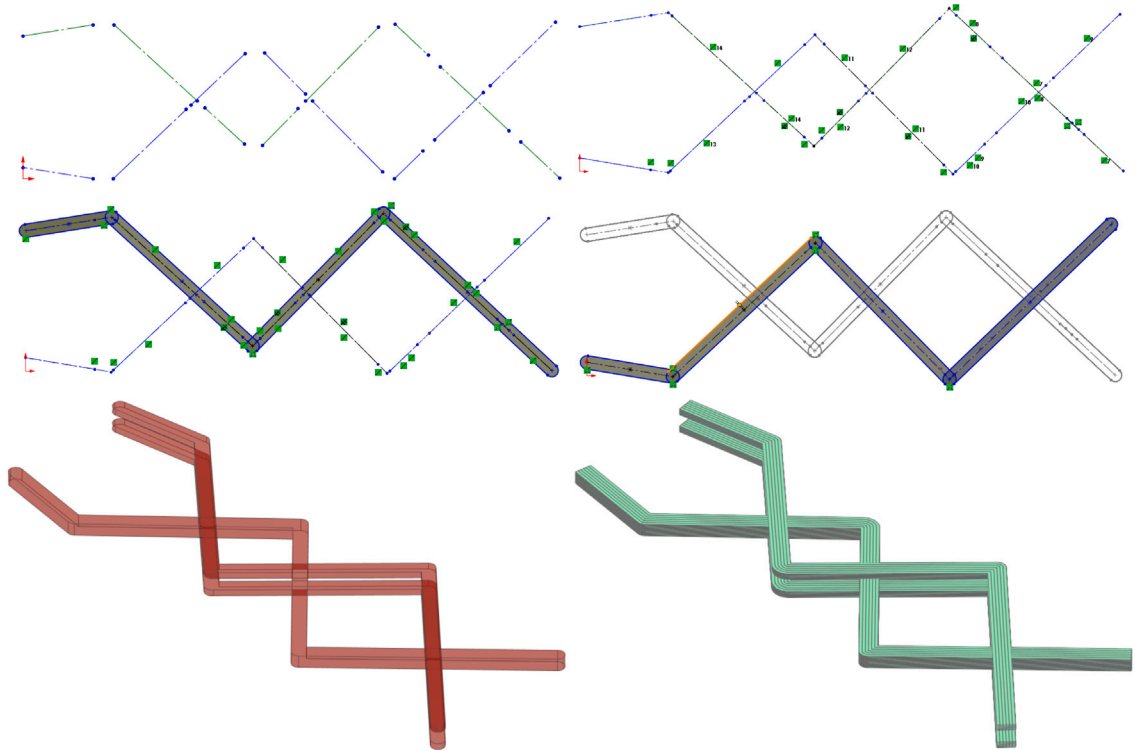


Fig. 8. The first row displays the bars' skeleton (left) of the optimized design (2<sup>nd</sup> row of Table 3), while the updated skeleton (right) is obtained by modifying the bars' endpoints. The second row depicts two CFFF trajectories obtained by modifying the bars' radii, ensuring fiber continuity in each layer while retaining the intersecting fiber trajectories in the design. The last row illustrates a symmetric solid-model interpretation (left) of the optimized design, while CFFF trajectories are created within Fibrify<sup>®</sup> on the right.

whose bars attain the upper bound on the radius. In the former case, since compliance is monotonic with volume, adding material will always decrease the compliance. However, since the bars cannot be made wider without violating the upper bound on the radius, a better design will be obtained by lengthening one or more bars, which will lead to an asymmetric design. In the latter case, the optimizer will shorten one or more bars to satisfy the volume constraint, again leading to an asymmetric design. It should be noted that this asymmetry is purely a result of the more restrictive design representation and not of the technique used to perform the analysis. The reader is referred to the discussion regarding symmetry in feature mapping methods in Wein et al. and the references therein.

It can also be observed that the optimization overlaps several bars around the point of load application, which is also expected.

#### 5.4. Rectangular plate under out-of-plane torsion and in-plane shear load cases

The fourth example considers a rectangular plate of dimensions 160 mm × 80 mm that is fixed on the left edge and subjected to two loads applied on the right edge and corresponding to two separate load cases. The design region is discretized using 160 × 80 bilinear, quadrilateral elements. The first load case consists of concentrated out-of-plane loads applied at the vertices of the right edge, resulting in an equivalent torque of 50 kN mm; the second load case corresponds to a downward load of 1 kN applied to the bottom right vertex. The boundary conditions and load cases are shown in Fig. 4. The initial design comprises 41 bars, and the design variables are subject to the following bounds:

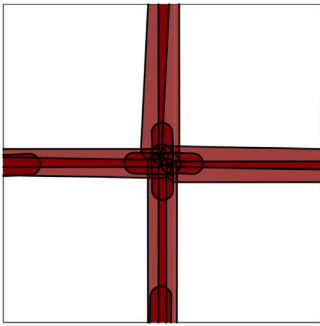
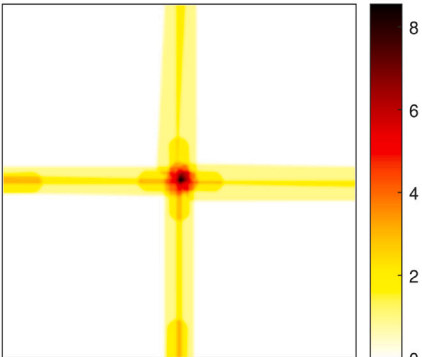
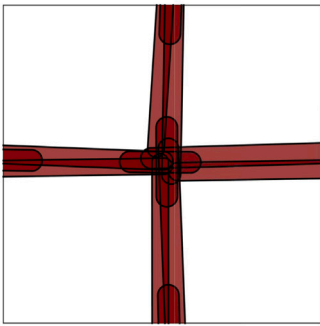
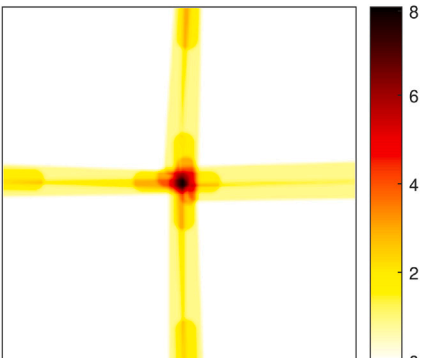
$$\begin{Bmatrix} (0, 0) \\ 2 \\ 0 \end{Bmatrix} \leq \begin{Bmatrix} (\mathbf{x}_{b1}, \mathbf{x}_{b2}) \\ r_b \\ \alpha_b \end{Bmatrix} \leq \begin{Bmatrix} (160, 80) \\ 5 \\ 1 \end{Bmatrix}. \tag{43}$$

In this example, we define the objective compliance function for the two load cases as the sum of the compliance for each load case, i.e.,  $c := \sum c_i$ , and the objective function is the same as before.

When printing a part using CF4, commonly imposed constraints on the fiber filament deposition include, among others, the minimum width of the reinforced features, the smallest reinforced area in each feature, and the minimum fiber length. The proposed method can readily accommodate these geometric constraints by imposing lower bounds on the bar's radius and length and, subsequently, all of the aforementioned quantities. While it is possible to impose a separate constraint in the optimization for the



**Table 4**  
Optimal designs and combined density for a square plate under out-of-plane point load.

$\underline{\ell}$ (mm)	$c$ (kN mm)	Design	Combined density
0	2.05		
12	2.03		

area of each bar, here we adopt the simpler approach that the lower bounds on the radius and the length of the bar satisfy the minimum area requirement. For this example, three different minimum length constraints  $\underline{\ell} = 0$  mm, 5 mm and 8 mm are imposed, with a fixed volume fraction limit  $\bar{v} = 0.4$ . The minimum reinforced area requirement corresponding to the length constraint and the lower bound on  $r_b$  is  $A_{\min} = 2r_b\underline{\ell} + \pi r_b^2$ . The foregoing values of the length constraint and the lower bound on radius listed in Eq. (43) are  $0$  mm<sup>2</sup>,  $32.56$  mm<sup>2</sup> and  $44.56$  mm<sup>2</sup>, respectively.

The optimization results for this example are shown in Table 5. The top row shows the LGP-AM design with no minimum length constraint, producing a design with an approximately symmetric topology and, as expected, several short bars. Note, however, that the design need not be symmetric because the second load case is not symmetric. The second and third rows of Table 5 correspond to the designs with  $\underline{\ell} = 5$  mm and 8 mm, respectively, which effectively eliminate short bars.

It should be noted that our numerical experiments indicate that the initial design has to be chosen so that all the bars satisfy the minimum length constraint. Otherwise, the optimizer will eliminate all bars in the first iterations of the optimization, leading to divergence.

### 5.5. Displacement inverter compliant mechanism

The last example corresponds to a displacement inverter design problem with a single input–output port. An input displacement  $u_{in}$  is prescribed at the input port modeled by a spring with stiffness  $k_{in} = 0.1$  kN/mm. The prescribed input displacement in turn produces an output displacement  $u_o$  at the output port, where again a spring with stiffness  $k_o = 0.1$  kN/mm is used to simulate the reaction force from the workpiece.

A fixed design domain of dimensions 80 mm×80 mm and the boundary conditions of the displacement inverter problem are shown in Fig. 4. The corners of the left-hand side edge are fixed, and an input displacement of  $u_{in} = 1$  mm is prescribed at the input port located at the midpoint of the left-hand side boundary; the output port is located at the midpoint of the right-hand side boundary of the design domain. Since the problem is symmetric, only the bottom half of the design region is optimized, and thus, symmetry boundary conditions are used for the analysis. The design region is discretized using  $80 \times 40$  bilinear quadrilateral elements. The volume fraction is set to 30%. The initial design consists of 22 bars, and the bounds imposed on the design variables are

$$\begin{Bmatrix} (0, 0) \\ 0.5 \\ 0 \end{Bmatrix} \leq \begin{Bmatrix} (\mathbf{x}_{b1}, \mathbf{x}_{b2}) \\ r_b \\ \alpha_b \end{Bmatrix} \leq \begin{Bmatrix} (80, 40) \\ 3 \\ 1 \end{Bmatrix}. \tag{44}$$

**Table 5**  
Optimal designs and combined density for the multi-load example.

$\underline{\ell}$ (mm)	$c$ (kN mm)	Design	Combined density
0	84.33		
5	84.41		
8	85.21		

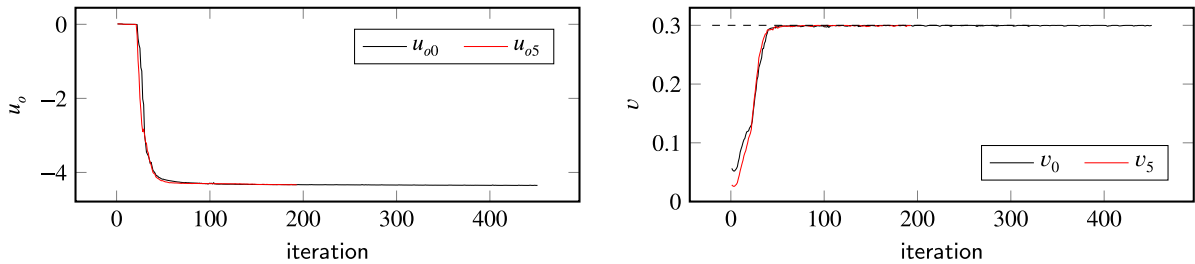


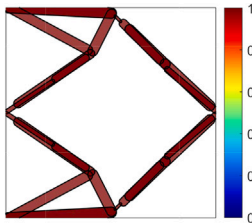
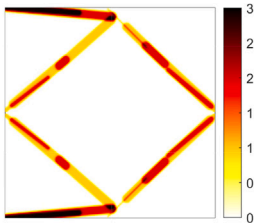
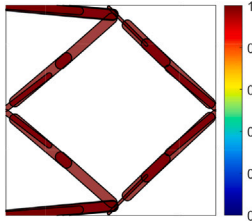
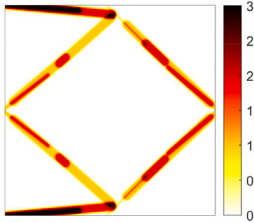
Fig. 9. Objective (left) and volume constraint (right) histories for the designs shown in Table 6 correspond to the LGP-AM designs.

Table 6 shows the optimal designs obtained with and without a minimum length constraint with the proposed method. Both optimizations produce designs similar to well-known solutions obtained using the density-based method. The design with no minimum length constraint (i.e.,  $\underline{\ell} = 0$  mm) renders short bars, and the design obtained with the minimum length constraint  $\underline{\ell} = 5$  mm does not produce short bars, as expected, again demonstrating the effectiveness of the length constraint. Fig. 9 shows that the optimization reaches the maximum number of iterations for the optimization without a length constraint, while significantly fewer iterations are needed to converge for the optimization with a minimum length constraint. This example illustrates that the minimum length constraint does not hamper the convergence behavior of the method when extended to consider other problems.

### 6. Conclusions

The numerical experiments presented demonstrate the effectiveness of the proposed LGP-AM for the topology optimization of VSCLs made of FRBs. The proposed computational technique is effective in its ability to produce competitive designs for minimum-compliance and linear compliant mechanism problems. The objective function histories indicate the proposed method converges smoothly, and it satisfies the convergence criteria in a number of iterations that are commensurate with that of other geometry projection techniques and density-based methods. The computational cost of the proposed method is also similar to that of other geometry projection techniques and density-based methods since the cost of the geometry projection is negligible compared to

**Table 6**  
Optimal designs and combined density for a displacement inverter problem.

$\ell$ (mm)	$u_o$ (mm)	Design	Combined density
0	-4.35		
5	-4.33		

the cost of the finite element analyses, as usual in topology optimization techniques. The robustness of the proposed method is demonstrated by solving several design problems with in-plane and/or out-of-plane loading conditions for different initial designs and arbitrary design domains, which consistently produced optimized designs that satisfied minimum-length constraints for the CF4 process. The examples demonstrated that the proposed minimum length constraint proposed in this work, which is based on penalization techniques and does not introduce additional constraints in the optimization problem, is effective and does not hamper the optimization convergence.

From a manufacturing point of view, the designs obtained with the proposed method are amenable to CF4 manufacturing techniques. Nevertheless, the designs produced by our method may require additional post-processing steps to reduce support structures; thus, an effective fiber path planning strategy (e.g., [66]) would be beneficial. Additionally, the proposed method is limited to a single-layer approach that does not consider the stacking sequence and thus underestimates the out-of-plane bending stiffness. Therefore, it is important to incorporate the stacking sequence in the optimization; this development will be addressed in future work.

**CRedit authorship contribution statement**

**Yogesh Gandhi:** Writing – review & editing, Writing – original draft, Visualization, Validation, Software, Methodology, Conceptualization. **Alejandro M. Aragón:** Writing – review & editing, Writing – original draft, Visualization, Supervision, Resources. **Julián Norato:** Writing – review & editing, Writing – original draft, Visualization, Validation, Supervision, Resources, Software, Methodology, Funding acquisition. **Giangiacomo Minak:** Writing – review & editing, Supervision, Resources, Project administration, Funding acquisition.

**Declaration of competing interest**

The authors declare that they have no known competing financial interests or personal relationships that could have appeared to influence the work reported in this paper.

**Acknowledgments**

The European Commission—NextGenerationEU supports this work through the National Sustainable Mobility Center, CN00000023 and the Italian Ministry of University and Research, 2022NW83RE\_002. The opinions expressed are those of the authors only and should not be considered representative of the European Union or the European Commission’s official position. Neither the European Union nor the European Commission can be held responsible for them.

The third author thanks the support of the United States National Science Foundation for conducting this work, Award CMMI-1751211.

## Appendix

### A.1. Distance function

The distance to the medial segment from  $\mathbf{x}$  is given by

$$d_b = \sqrt{(d_b^\perp)^2 + (d_b^\parallel)^2},$$

where,

$$\begin{aligned} d_b^\perp &= \|\mathbf{P}_b^\perp \mathbf{x}_b\| & d_b^\parallel &= \max \left\{ 0, \|\mathbf{P}_b^\parallel \mathbf{x}_b\| - \frac{\|\mathbf{v}_b\|}{2} \right\} \\ \mathbf{P}_b^\perp &= \mathbf{I} - \mathbf{P}_b^\parallel & \mathbf{P}_b^\parallel &:= \frac{\mathbf{v}_b \otimes \mathbf{v}_b}{\|\mathbf{v}_b\|^2} \\ \mathbf{x}_b &:= \mathbf{x} - \mathbf{x}_{1b} & \mathbf{v}_b &:= \mathbf{x}_{2b} - \mathbf{x}_{1b} \end{aligned}$$

In these expressions,  $\mathbf{P}_b^\perp$  and  $\mathbf{P}_b^\parallel$  denote the perpendicular and parallel projectors to the medial axis vector  $\mathbf{v}_b$  of bar  $b$ , respectively, and  $\otimes$  denotes the tensor product.

### A.2. Smooth functions

The regularized Heaviside and softargmax functions used in the formulation and their sensitivities are given by:

$$\tilde{H}(x) = \begin{cases} 0, & \text{if } x \leq -1 \\ 1 + \frac{1}{\pi} \left( x\sqrt{1-x^2} - \arccos x \right), & \text{if } |x| < 1 \\ 1, & \text{if } x \geq 1 \end{cases}$$

$$\frac{d\tilde{H}}{dx} = \begin{cases} 2\sqrt{1-x^2}/\pi, & \text{if } |x| < 1 \\ 0, & \text{otherwise} \end{cases}$$

$$w_i(\mathbf{x}) = \widetilde{\text{argmax}}_j(x_j; \beta) = \frac{e^{\beta x_i}}{\sum_j e^{\beta x_j}}$$

$$\frac{\partial w_i}{\partial x_j} = \beta w_i (\delta_{ij} - w_j)$$

The error function, often denoted by erf, is defined as

$$\text{erf } z = \frac{2}{\sqrt{\pi}} \int_0^z e^{-t^2} dt$$

$$\frac{d}{dz} \text{erf } z = \frac{2}{\sqrt{\pi}} e^{-z^2}$$

(45)

## Data availability

Data will be made available on request.

## References

- [1] S.F. Kabir, K. Mathur, A.-F.M. Seyam, A critical review on 3D printed continuous fiber-reinforced composites: History, mechanism, materials and properties, *Compos. Struct.* 232 (2020) 111476, <https://doi.org/10.1016/j.compstruct.2019.111476>.
- [2] A. Brasington, C. Sacco, J. Halbritter, R. Wehbe, R. Harik, Automated fiber placement: A review of history, current technologies, and future paths forward, *Composites C* 6 (2021) 100182, <https://doi.org/10.1016/j.jcomc.2021.100182>.
- [3] Z. Hong, D. Peeters, S. Turteltaub, An enhanced curvature-constrained design method for manufacturable variable stiffness composite laminates, *Comput. Struct.* 238 (2020) 106284, <https://doi.org/10.1016/j.compstruc.2020.106284>.
- [4] T. Shafighard, E. Demir, M. Yildiz, Design of fiber-reinforced variable-stiffness composites for different open-hole geometries with fiber continuity and curvature constraints, *Compos. Struct.* 226 (2019) 111280, <https://doi.org/10.1016/j.compstruct.2019.111280>.
- [5] D.M. Peeters, S. Hesse, M.M. Abdalla, Stacking sequence optimisation of variable stiffness laminates with manufacturing constraints, *Compos. Struct.* 125 (2015) 596–604, <https://doi.org/10.1016/j.compstruct.2015.02.044>.
- [6] I. 9T LABS, 9T LABS 3D printer: How it works, 2024, <https://www.9tlabs.com/how-it-works>. (Accessed 15 October 2024).
- [7] I. Markforged, Markforged mark two 3D printer, 2024, <https://markforged.com/3d-printers/mark-two>. (Accessed 15 October 2024)).
- [8] D. Peeters, M. Abdalla, Optimization of ply drop locations in variable-stiffness composites, *AIAA J.* 54 (5) (2016) 1760–1768, <https://doi.org/10.2514/1.J054369>.

- [9] I. Markforged, Markforged mark two 3D printer, 2024, [https://s3.amazonaws.com/mf.product.doc.images/Composites\\_DesignGuide/CompositesDesignGuide.pdf](https://s3.amazonaws.com/mf.product.doc.images/Composites_DesignGuide/CompositesDesignGuide.pdf). (Accessed 15 October 2024).
- [10] X. Tian, T. Liu, C. Yang, Q. Wang, D. Li, Interface and performance of 3D printed continuous carbon fiber reinforced PLA composites, *Composites A* 88 (2016) 198–205, <https://doi.org/10.1016/j.compositesa.2016.05.032>.
- [11] Q. He, H. Wang, K. Fu, L. Ye, 3D printed continuous CF/PA6 composites: Effect of microscopic voids on mechanical performance, *Compos. Sci. Technol.* 191 (2020) 108077, <https://doi.org/10.1016/j.compscitech.2020.108077>.
- [12] H. Ghiasi, D. Pasini, L. Lessard, Optimum stacking sequence design of composite materials Part I: Constant stiffness design, *Compos. Struct.* 90 (2009) 1–11, <http://dx.doi.org/10.1016/j.compstruct.2009.01.006>.
- [13] H. Ghiasi, K. Fayazbakhsh, D. Pasini, L. Lessard, Optimum stacking sequence design of composite materials Part II: Variable stiffness design, *Compos. Struct.* 93 (2010) 1–13, <https://doi.org/10.1016/j.compstruct.2010.06.001>.
- [14] J. Plocher, A. Panesar, Review on design and structural optimisation in additive manufacturing: Towards next-generation lightweight structures, *Mater. Des.* 183 (2019) 108164, <http://dx.doi.org/10.1016/j.matdes.2019.108164>.
- [15] M.P. Bendsoe, O. Sigmund, *Topology Optimization: Theory, Methods, and Applications*, Springer Science & Business Media, 2004.
- [16] G.I.N. Rozvany, A critical review of established methods of structural topology optimization, *Struct. Multidiscip. Optim.* 37 (2009) 217–237, <https://doi.org/10.1007/s00158-007-0217-0>.
- [17] O. Sigmund, K. Maute, Topology optimization approaches, *Struct. Multidiscip. Optim.* 48 (6) (2013) 1031–1055, <https://doi.org/10.1007/s00158-013-0978-6>.
- [18] N.P. Van Dijk, K. Maute, M. Langelaar, F. Van Keulen, Level-set methods for structural topology optimization: A review, *Struct. Multidiscip. Optim.* 48 (2013) 437–472, <https://doi.org/10.1007/s00158-013-0912-y>.
- [19] J.D. Deaton, R.V. Grandhi, A survey of structural and multidisciplinary continuum topology optimization: Post 2000, *Struct. Multidiscip. Optim.* 49 (2014) 1–38, <https://doi.org/10.1007/s00158-013-0956-z>.
- [20] Y. Gandhi, G. Minak, A review on topology optimization strategies for additively manufactured continuous fiber-reinforced composite structures, *Appl. Sci.* 12 (21) (2022) 11211, <https://doi.org/10.3390/app122111211>.
- [21] D. Jiang, R. Høglund, D.E. Smith, Continuous fiber angle topology optimization for polymer composite deposition additive manufacturing applications, *Fibers* 7 (2) (2019) 14, <https://doi.org/10.3390/fib7020014>.
- [22] M.P. Schmidt, L. Couret, C. Gout, C.B. Pedersen, Structural topology optimization with smoothly varying fiber orientations, *Struct. Multidiscip. Optim.* 62 (2020) 3105–3126, <https://doi.org/10.1007/s00158-020-02657-6>.
- [23] X. Yan, Q. Xu, H. Hua, D. Huang, X. Huang, Concurrent topology optimization of structures and orientation of anisotropic materials, *Eng. Optim.* 52 (2020) 1598–1611, <https://doi.org/10.1080/0305215X.2019.1663186>.
- [24] Y. Lu, L. Tong, Concurrent optimization of topologies and fiber orientations for laminated composite structures, *Compos. Struct.* (2022) 115749, <https://doi.org/10.1016/j.compstruct.2022.115749>.
- [25] Y. Tian, S. Pu, T. Shi, Q. Xia, A parametric divergence-free vector field method for the optimization of composite structures with curvilinear fibers, *Comput. Methods Appl. Mech. Engrg.* 373 (2021) 113574, <https://doi.org/10.1016/j.cma.2020.113574>.
- [26] C.J. Brampton, K.C. Wu, H.A. Kim, New optimization method for steered fiber composites using the level set method, *Struct. Multidiscip. Optim.* 52 (2015) 493–505, <https://doi.org/10.1007/s00158-015-1256-6>.
- [27] F. Fernandez, W.S. Compel, J.P. Lewicki, D.A. Tortorelli, Optimal design of fiber reinforced composite structures and their direct ink write fabrication, *Comput. Methods Appl. Mech. Engrg.* 353 (2019) 277–307, <https://doi.org/10.1016/j.cma.2019.05.010>.
- [28] V.S. Papapetrou, C. Patel, A.Y. Tamijani, Stiffness-based optimization framework for the topology and fiber paths of continuous fiber composites, *Composites B* 183 (2020) 107681, <https://doi.org/10.1016/j.compositesb.2019.107681>.
- [29] J. Stegmann, E. Lund, Discrete material optimization of general composite shell structures, *Internat. J. Numer. Methods Engrg.* 62 (14) (2005) 2009–2027, <https://doi.org/10.1002/nme.1259>.
- [30] S.N. Sørensen, R. Sørensen, E. Lund, DMTO—a method for discrete material and thickness optimization of laminated composite structures, *Struct. Multidiscip. Optim.* 50 (1) (2014) 25–47, <https://doi.org/10.1007/s00158-014-1047-5>.
- [31] R. Sørensen, E. Lund, Thickness filters for gradient based multi-material and thickness optimization of laminated composite structures, *Struct. Multidiscip. Optim.* 52 (2) (2015) 227–250, <https://doi.org/10.1007/s00158-015-1230-3>.
- [32] J. Sjølund, D. Peeters, E. Lund, A new thickness parameterization for discrete material and thickness optimization, *Struct. Multidiscip. Optim.* 58 (5) (2018) 1885–1897, <https://doi.org/10.1007/s00158-018-2093-1>.
- [33] D. Hozjić, C.-J. Thore, C. Cameron, M. Loukil, A new method for simultaneous material and topology optimization of composite laminate structures using hyperbolic function parametrization, *Compos. Struct.* 276 (2021) 114374, <https://doi.org/10.1016/j.compstruct.2021.114374>.
- [34] C. Forward, I.Y. Kim, Layered fiber orientation optimization for continuous fiber reinforced polymer additive manufacturing using multi-material topology optimization, *Prog. Addit. Manuf.* (2023) 1–12, <https://doi.org/10.1007/s40964-023-00434-7>.
- [35] E. Lund, Discrete material and thickness optimization of laminated composite structures including failure criteria, *Struct. Multidiscip. Optim.* 57 (2018) 2357–2375, <https://doi.org/10.1007/s00158-017-1866-2>.
- [36] T. Nomura, E.M. Dede, J. Lee, S. Yamasaki, T. Matsumori, A. Kawamoto, N. Kikuchi, General topology optimization method with continuous and discrete orientation design using isoparametric projection, *Internat. J. Numer. Methods Engrg.* 101 (2015) 571–605, <https://doi.org/10.1002/nme.4799>.
- [37] C.Y. Kiyono, E.C.N. Silva, J.N. Reddy, A novel fiber optimization method based on normal distribution function with continuously varying fiber path, *Compos. Struct.* 160 (2017) 503–515, <https://doi.org/10.1016/j.compstruct.2016.10.064>.
- [38] Y. Luo, W. Chen, S. Liu, Q. Li, Y. Ma, A discrete-continuous parameterization (DCP) for concurrent optimization of structural topologies and continuous material orientations, *Compos. Struct.* 236 (2020) 111900, <https://doi.org/10.1016/j.compstruct.2020.111900>.
- [39] Z. Qiu, Q. Li, Y. Luo, S. Liu, Concurrent topology and fiber orientation optimization method for fiber-reinforced composites based on composite additive manufacturing, *Comput. Methods Appl. Mech. Engrg.* 395 (2022) 114962, <https://doi.org/10.1016/j.cma.2022.114962>.
- [40] Z. Yang, K. Fu, Z. Zhang, J. Zhang, Y. Li, Topology optimization of 3D-printed continuous fiber-reinforced composites considering manufacturability, *Compos. Sci. Technol.* 230 (2022) 109727, <https://doi.org/10.1016/j.compscitech.2022.109727>.
- [41] L. Yin, G.K. Ananthasuresh, A novel topology design scheme for the multi-physics problems of electro-thermally actuated compliant micromechanisms, *Sensors Actuators A* 97 (2002) 599–609, [https://doi.org/10.1016/S0924-4247\(01\)00853-6](https://doi.org/10.1016/S0924-4247(01)00853-6).
- [42] F. Fernandez, W.S. Compel, J.P. Lewicki, D.A. Tortorelli, Optimal design of fiber reinforced composite structures and their direct ink write fabrication, *Comput. Methods Appl. Mech. Engrg.* 353 (2019) 277–307, <https://doi.org/10.1016/j.cma.2019.05.010>.
- [43] Y. Chen, L. Ye, Topological design for 3D-printing of carbon fibre reinforced composite structural parts, *Compos. Sci. Technol.* 204 (2021) 108644, <https://doi.org/10.1016/j.compscitech.2020.108644>.
- [44] T. Wang, N. Li, G. Link, J. Jelonnek, J. Fleischer, J. Dittus, D. Kupzik, Load-dependent path planning method for 3D printing of continuous fiber reinforced plastics, *Composites A* 140 (2021) 106181, <https://doi.org/10.1016/j.compositesa.2020.106181>.
- [45] B. Fedulov, A. Fedorenko, A. Khaziev, F. Antonov, Optimization of parts manufactured using continuous fiber three-dimensional printing technology, *Composites B* 227 (2021) 109406, <https://doi.org/10.1016/j.compositesb.2021.109406>.

- [46] P. Parandoush, D. Lin, A review on additive manufacturing of polymer-fiber composites, *Compos. Struct.* 182 (2017) 36–53, <https://doi.org/10.1016/j.compstruct.2017.08.088>.
- [47] F. Wein, P.D. Dunning, J.A. Norato, A review on feature-mapping methods for structural optimization, *Struct. Multidiscip. Optim.* 62 (2020) 1597–1638, <https://doi.org/10.1007/s00158-020-02649-6>.
- [48] J.A. Norato, B.K. Bell, D.A. Tortorelli, A geometry projection method for continuum-based topology optimization with discrete elements, *Comput. Methods Appl. Mech. Engrg.* 293 (2015) 306–327, <https://doi.org/10.1016/j.cma.2015.05.005>.
- [49] H. Smith, J.A. Norato, Topology optimization with discrete geometric components made of composite materials, *Comput. Methods Appl. Mech. Engrg.* 376 (2021) 113582, <https://doi.org/10.1016/j.cma.2020.113582>.
- [50] H. Smith, J. Norato, Topology optimization of structures made of fiber-reinforced plates, *Struct. Multidiscip. Optim.* 65 (2) (2022) 58, <https://doi.org/10.1007/s00158-021-03164-y>.
- [51] H. Smith, J. Norato, Simultaneous material and topology optimization of composite laminates, *Comput. Methods Appl. Mech. Engrg.* 404 (2023) 115781, <https://doi.org/10.1016/j.cma.2022.115781>.
- [52] Y. Zhou, T. Nomura, K. Saitou, Multi-component topology and material orientation design of composite structures (MTO-C), *Comput. Methods Appl. Mech. Engrg.* 342 (2018) 438–457, <https://doi.org/10.1016/j.cma.2018.07.039>.
- [53] J.N. Reddy, *Mechanics of laminated composite plates- Theory and analysis(Book)*, 1997.
- [54] H. Smith, J.A. Norato, A MATLAB code for topology optimization using the geometry projection method, *Struct. Multidiscip. Optim.* 62 (3) (2020) 1579–1594, <https://doi.org/10.1007/s00158-020-02552-0>.
- [55] M.P. Bendsøe, O. Sigmund, Material interpolation schemes in topology optimization, *Arch. Appl. Mech.* 69 (1999) 635–654, <https://doi.org/10.1007/s004190050248>.
- [56] J. Aboudi, S.M. Arnold, B.A. Bednarczyk, *Practical Micromechanics of Composite Materials*, Butterworth-Heinemann, 2021.
- [57] J. Reddy, A. Srinivasa, Misattributions and misnomers in mechanics: Why they matter in the search for insight and precision of thought, *Vietnam J. Mech.* 42 (2020) 283–291, <https://doi.org/10.15625/0866-7136/15476>.
- [58] J. Zhou, G. Zhao, Y. Zeng, G. Li, A novel topology optimization method of plate structure based on moving morphable components and grid structure, *Struct. Multidiscip. Optim.* 67 (1) (2024) 1–19, <https://doi.org/10.1007/s00158-023-03719-1>.
- [59] S. Zhang, J.A. Norato, A.L. Gain, N. Lyu, A geometry projection method for the topology optimization of plate structures, *Struct. Multidiscip. Optim.* 54 (2016) 1173–1190, <https://doi.org/10.1007/s00158-016-1466-6>.
- [60] J. Petersson, A finite element analysis of optimal variable thickness sheets, *SIAM J. Numer. Anal.* 36 (6) (1999) 1759–1778, <https://doi.org/10.1137/S0036142996313968>.
- [61] K. Svanberg, The method of moving asymptotes—a new method for structural optimization, *Internat. J. Numer. Methods Engrg.* 24 (1987) 359–373, <https://doi.org/10.1002/nme.1620240207>.
- [62] K. Svanberg, MMA and GCMMA, versions september 2007, *Optim. Syst. Theory* 104 (2007) <https://people.kth.se/~krille/gcmmma07.pdf>.
- [63] P. Pedersen, Some general optimal design results using anisotropic, power law nonlinear elasticity, *Struct. Optim.* 15 (1998) 73–80, <https://doi.org/10.1007/BF01278492>.
- [64] N.L. Pedersen, On topology optimization of plates with prestress, *Internat. J. Numer. Methods Engrg.* 51 (2) (2001) 225–239.
- [65] N. Boddeti, Y. Tang, K. Maute, D.W. Rosen, M.L. Dunn, Optimal design and manufacture of variable stiffness laminated continuous fiber reinforced composites, *Sci. Rep.* 10 (1) (2020) 1–15, <https://doi.org/10.1038/s41598-020-73333-4>.
- [66] F. Wein, J. Mirbach, A. Angre, J. Greifenstein, D. Hübner, Multi-layer continuous carbon fiber pattern optimization and a spline based path planning interpretation, 2024, arXiv preprint [arXiv:2404.11404](https://arxiv.org/abs/2404.11404).